Scaled testing of maximum-reserve active power control

Simone Tamaro, Davide Bortolin, Filippo Campagnolo, Franz V. Mühle, and Carlo L. Bottasso

Wind Energy Institute, Technical University of Munich, 85748 Garching b. München, Germany

Correspondence: Carlo L. Bottasso (carlo.bottasso@tum.de)

Abstract.

We present the scaled experimental validation of an active power control (APC) algorithm designed to optimize the tracking accuracy of a wind farm in the presence of turbulent wind lulls. This is obtained by maximizing the minimum local power availability (called reserve) across the farm. This method combines an offline-computed open-loop setpoint scheduler aimed at the power reserves, with a fast closed-loop corrector tasked with enhancing tracking accuracy. The open-loop component is synthesized using an augmented version of FLORIS, which models the combined effects of yaw misalignment and power curtailment, wind tunnel-specific inflow characteristics, and the influence of the chord-based Reynolds number (caused by the small size of the models) on the performance of the rotors.

A preliminary simulation-based steady-state analysis indicates that the approach effectively enhances local power availability across the wind farm by leveraging both induction and wake steering control. The methodology is then experimentally demonstrated in a large boundary-layer wind tunnel with minimal blockage, in different scenarios, including dynamically varying wind direction conditions. Its performance is benchmarked against three alternative APC strategies sourced from the literature. During the experiments, the APC algorithms run in real time on a dedicated cabinet and communicate with the turbine controllers via a dedicated network. Dynamic wind direction changes are generated using a large turntable driven by a field-recorded wind direction time series, scaled to match the temporal dynamics of the wind tunnel.

Results show that in both static and dynamic scenarios, the proposed control strategy outperforms the reference methods in power tracking accuracy, particularly under high power demand conditions, while maintaining a limited impact on structural fatigue. Notably, the algorithm effectively manages wake interactions and redistributes local power demands to increase local power reserves, thereby mitigating saturation effects and improving overall tracking performance.

1 Introduction

Active Power Control (APC) is a key area of wind farm control that has attracted a growing interest in the context of the ongoing energy transition (Aho et al., 2012; Ela et al., 2014). In regions with high wind energy penetration, wind farms are increasingly required to contribute to grid stability (Boyle and Littler, 2024). This can be accomplished at different time scales that span from the order of seconds (inertia control and primary frequency control) to minutes (secondary frequency control). In the secondary frequency control regime, a wind farm must adjust its total power output according to the requests of the transmission system operator (TSO) (Aho et al., 2012).

In recent years, extensive research has focused on developing wind farm control strategies aimed at increasing the collective power output of turbines. Common approaches include wake redirection (Jiménez et al., 2010; Campagnolo et al., 2016; Fleming et al., 2019; Doekemeijer et al., 2021; Nanos et al., 2022), static and dynamic induction control (Munters and Meyers, 2018; van der Hoek et al., 2019; Frederik et al., 2020b; Bossanyi and Ruisi, 2021), and, more recently, wake mixing (Frederik et al., 2020a; Mühle et al., 2024; Lin and Porté-Agel, 2024).

Wind farm active power control (APC), however, differs in a fundamental way from these power-boosting strategies. In fact, wind farms in APC operation are required to operate in curtailed mode, producing less than the maximum power that they could generate in the present ambient conditions. This mode of operation introduces new control challenges. For instance, how should a turbine be controlled to curtail its power output? How is its wake affected by power curtailment, and can turbines be controlled collectively to benefit power tracking accuracy? Is the effectiveness of wake redirection methods modified by off-rated operation? And what are the consequences in terms of structural fatigue?

Some of these and other questions have already been addressed in the literature. For example, Fleming et al. (2016) highlighted the limits of open-loop APC methods for wind farms, and van Wingerden et al. (2017) showed that a closed-loop control architecture can effectively minimize power tracking errors. Gonzalez Silva et al. (2022) later extended this work and stressed the importance of addressing saturation events (i.e. conditions in which the local power demand exceeds the local power availability) to avoid negatively affecting power tracking accuracy. Vali et al. (2019) demonstrated the pairing of power tracking with a side goal, and specifically with the limitation of structural fatigue. The authors achieved this result by adopting a special power demand distribution across the farm, and demonstrated their approach with actuator-disk large eddy simulations (LES). More recently Starke et al. (2023) and Oudich et al. (2023) have paired APC with wake steering, showing that the time scales required by wake redirection are compatible with secondary grid frequency regulation. However, these studies lack a comprehensive modeling of misaligned operation conditions – which are significantly affected by curtailment (Cossu, 2021; Heck et al., 2023) – and a dynamic analysis of wind direction variability.

So far, most work on APC has been carried out numerically. Two instances of experimental APC tests have been presented by Petrović et al. (2018) and Gonzalez Silva et al. (2024). Petrović et al. (2018) considered a small cluster of two rotors in two wind direction scenarios. Their study demonstrated the strong effects played by the power share distribution on tracking accuracy and structural fatigue, and by wake effects, especially in partial rotor overlap conditions. In their work, the flow was almost laminar and the turbines relied only on torque control to curtail their power output, which is not necessarily realistic. Gonzalez Silva et al. (2024) later considered a cluster of three turbines in full alignment conditions and tested two APC techniques. The authors showed the importance of saturation events in determining tracking accuracy, and highlighted their difficult treatment with load-balancing approaches in high power demand conditions. That same paper also investigated two distinct wind turbine control approaches for off-rated operation, resulting in different wake characteristics, which in turn affect the local power availability at downstream rotors.

Neither experimental nor numerical APC studies have yet accounted for wind direction variability. Wind direction changes occur naturally in any wind farm site and heavily influence wake-rotor interactions (Porté-Agel et al., 2013).

In this paper, we experimentally validate the wind farm APC maximum-reserve method presented in Tamaro et al. (2025b), where this approach was developed and analyzed by means of numerical simulations. Here, the algorithm is tested using a cluster of scaled wind turbines operating in a large boundary-layer wind tunnel, where varying wind directions are used to replicate some of the dynamic effects happening in the field. By exploiting the fact that time flows much faster in a scaled experiment than at full scale (Canet et al., 2021; Bottasso and Campagnolo, 2022) – with a speedup larger than 80 in the present case – this work overcomes the limited duration of the simulations in our previous numerical study.

The wind tunnel campaign presented in this work improves on some preliminary tests that we reported in Tamaro et al. (2024b). Compared to that work, here we have extended the operating conditions, refined the APC algorithms, and expanded the analysis of the results with additional metrics, which now include saturation events and structural fatigue.

The paper is organized as follows: Sect. 2 briefly reviews the formulation of the maximum-reserve controller and of three additional APC methods for performance comparisons, Sect. 3 describes the experimental setup, and Sect. 4 details the steady-state simulation environment used to synthesize the controller setpoints. Experimental results are reported and discussed in Sect. 5 for scenarios with fixed wind directions, and in Sect. 6 for dynamic wind direction conditions. Finally, Sect. 7 draws conclusions and offers an outlook towards future work.

2 Active power control formulation

2.1 Closed-loop with maximum reserve (CL + MR)

The maximum-reserve APC used in this work has been extensively described in Tamaro et al. (2025b), so here we only summarize its main features. The core of the wind farm control architecture is an open-loop model-based setpoint optimal scheduler that determines the yaw misalignment and power demand of each turbine, given the power demand required by the TSO and the ambient conditions. Furthermore, a feedback loop serves the purpose of correcting tracking errors that may arise from the open loop in real time. A sketch of the controller is shown in Fig. 1.

The closed and open loops are executed at two distinct time rates, since their outputs involve physical phenomena characterized by different time scales. Specifically, the open loop updates the yaw setpoints γ_i and the power demand P_D at a slow pace, due to the time required by wakes to propagate downstream, whereas the closed-loop corrector acts at a rate that is two orders of magnitude faster.

2.1.1 Open-loop setpoint optimal scheduler

The open-loop component of the algorithm provides the optimal setpoints in terms of yaw misalignment and power share. These are computed by a gradient-based optimization that maximizes the smallest power reserve within the farm for a given overall power demand and ambient conditions.

Given the total number of turbines N in the farm, the power of the i-th machine is noted $P_i = P_i(\mathbf{A}_i, \mathbf{u}_i)$, where $\mathbf{A}_i$ indicates the ambient conditions. Ambient conditions here are assumed to include freestream wind speed U_∞, wind direction ψ, vertical
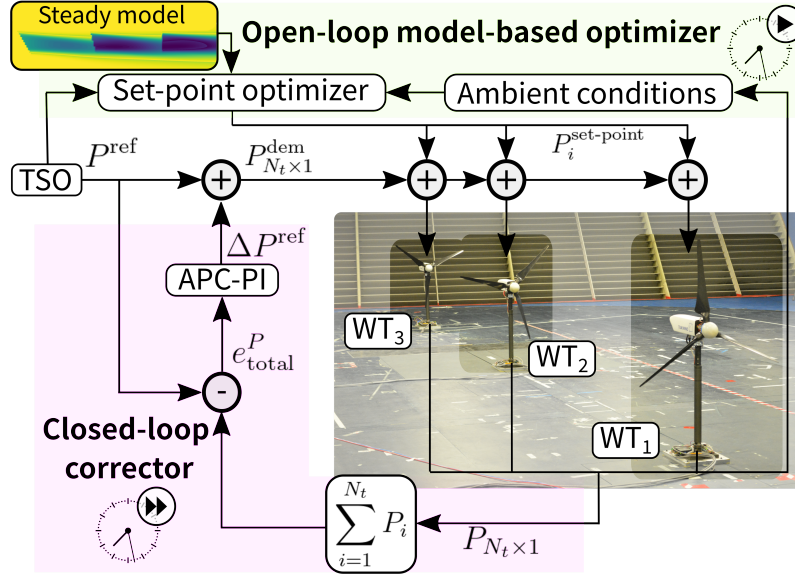
Figure 1. Schematic representation of the maximum-reserve APC controller, featuring an open-loop model-based optimizer and a closed-loop corrector.

shear k, and turbulence intensity (TI) I. The control inputs are noted $\mathbf{u}_i$, and they include the power share $\alpha_i = P_i / \sum_{i=1}^{N} P_i$ and yaw misalignment γ_i.

The maximum power that can be generated by turbine i by adjusting its control setpoints $\mathbf{u}_i$ (while keeping the setpoints of the other turbines fixed) in the ambient conditions $\mathbf{A}_i$ is computed as

$$P_{a,i} = \max_{\mathbf{u}_i} P_i(\mathbf{A}_i, \mathbf{u}_i) = \frac{1}{2} \rho \pi R^2 U^3 C_P \eta_P(\gamma_i, \delta_i),$$

where ρ is the air density, C_P is the power coefficient, R is the rotor radius, U is the local rotor-equivalent wind speed, and η_P is the power scaling factor used by Tamaro et al. (2024a) to model power losses due to yaw γ and tilt δ. The local flow conditions at the rotor of a turbine, including U, are computed with an engineering flow model, here based on FLORIS (National Renewable Energy Laboratory, 2022). The power tracking method looks for the combination of setpoints that produce the minimum possible maximum power ratio $P_i/P_{a,i}$ across all N turbines in the farm while satisfying the power demand of the TSO, P_{ref}. This tracking criterion can be expressed as

$$\min_{\mathbf{u}} \max_{i \in [1,N]} \frac{P_i}{P_{a,i}}, \tag{1a}$$

$$\text{such that: } \sum_{i=1}^{N} P_i = P_{\text{ref}}. \tag{1b}$$

In fact, the smaller the power ratio $P_i/P_{a,i}$, the larger the reserve $1 - P_i/P_{a,i}$ that is available to compensate against drops in the wind.

Equation (1) represents a constrained optimization problem. The optimization does not need to be performed in real-time during operation. Rather, it is executed offline for a set of ambient conditions and levels of wind farm curtailment. Results are collected in a lookup table (LUT), which is then interpolated at run-time, similarly to what is routinely done for power-boosting wind farm control (Meyers et al., 2022), so that

$$\alpha_i = \alpha_i(P_{\text{ref}}, \psi, U_\infty, k, I) \tag{2a}$$

$$\gamma_i = \gamma_i(P_{\text{ref}}, \psi, U_\infty, k, I). \tag{2b}$$

2.1.2 Closed-loop corrector

The closed-loop corrector is directly taken from the work of van Wingerden et al. (2017). The corrector consists of a simple proportional-integral (PI) feedback loop that operates on the power tracking error, which arises from the open-loop component of the control structure. Its goal is to ensure that as some turbines deviate from their respective demands, the reference power tracking signal is promptly corrected.

The tracking error Δ_P is defined as

$$\Delta_P = P_{\text{ref}} - \sum_{i=1}^{N} P_i. \tag{3}$$

The control signal $P_{\text{ref}}^{\text{PI}}$ at time instant τ is defined as

$$P_{\text{ref}}^{\text{PI}} = K_{APC}^{P} \Delta_{P,\tau} + K_{APC}^{I} \sum_{j=1}^{\tau} \Delta_{P,j}, \tag{4}$$

where K_{APC}^{P} and K_{APC}^{I} are the PI gains, and j a time step counter. The wind farm is then required to track $P_{\text{ref}} + P_{\text{ref}}^{\text{PI}}$.

The PI gains are obtained with a tuning procedure based on the simple SIMULINK (The MathWorks, Inc., 2022) model described in Sect. 3.4. The controller features an anti-windup element on the integrator when all turbines are saturated, i.e. when $S = N$, where S denotes the number of saturated rotors. Furthermore, the integrator is reset in certain conditions, as described in Sect. 3.4. The gain scheduling based on the number of saturated turbines proposed by van Wingerden et al. (2017) is not used due to the small size of the farm considered here, which causes abrupt variations in the gains that can lead to instabilities. Instead, when a turbine saturates, its local power tracking error is redistributed equally among the non-saturated ones as proposed by Vali et al. (2019) and described in more detail in Sect. 2.4.

2.2 Reference APC formulations for performance comparison

We rely on three reference wind farm APC controllers to compare the performance of the maximum-reserve method, namely:

– **Open-loop (OL):** this simple approach assigns predetermined setpoints α_i to each turbine, as fractions of the power demanded by the TSO, so that $\sum_{i=1}^{N} \alpha_i = 1$. The setpoints α_i are scheduled with the instantaneous wind direction, so that $\alpha_i = \alpha_i(\psi)$ to account for different local power availabilities induced by wake impingements. The values α_i are computed with the FLORIS model (National Renewable Energy Laboratory, 2022), as described in Sect. 4.

– **Closed-loop (CL)**: this method is the same as OL with the addition of the closed-loop PI corrector described in Sect. 2.1.2. Similarly to the OL method, the values α_i are scheduled with the instantaneous wind direction based on predictions from FLORIS.

– **Closed-loop with load balance (CL + LB)**: this method consists of CL without the fixed scheduling of the power share setpoints α_i. Instead, an additional PI loop is nested to distribute the setpoints α_i with the goal of balancing loads within the wind farm (Vali et al., 2019). This coordinated load distribution (CLD) loop modifies the power share setpoints to minimize the load balancing error ΔL, which is defined as

$$\Delta_{L,i} = L_i - \overline{L}, \tag{5}$$

where L_i is the load of the i-th turbine and $\overline{L} = \frac{1}{N-S} \sum_{i=1}^{N-S} L_{i,\text{non sat.}}$ is the average load in the farm. A PI power share distribution at time instant τ is computed as

$$\alpha_{i,\tau} = K_{CLD}^P \Delta_{L,i} + K_{CLD}^I \sum_{j=1}^{\tau} \Delta_{L,i,j}, \tag{6}$$

where K_{CLD}^P and K_{CLD}^I are the PI gains.

In this work, the tower base fore-aft bending moment is chosen as the target load L. The PI gains of the CLD loop are tuned with the same SIMULINK model used for the APC loop, described in Sect. 3.4. As proposed by Gonzalez Silva et al. (2022), the mean load is computed considering only non-saturated turbines. Furthermore, the integrator is reset on all turbines in the event that all turbines reach saturation. In these conditions, the error $\Delta_{L,i}$ is null – since it is computed only with non-saturated turbines – and the integrator component lies at zero, until at least one turbine recovers from saturation. An anti-windup is finally added to the integrator of each turbine whenever the power share α exceeds unfeasible values.

It is important to mention that the setpoints for CL+MR are computed using the same FLORIS version adopted for OL, CL, and CL+LB. This ensures that any discrepancy deriving from the steady state model is present in each compared control approach. Furthermore, CL, CL+LB and CL+LB feature the same PI control block described in Sect. 2.1.2, ensuring that the closed-loop element is also the same.

2.3 Wind turbine controller

The wind turbine controller is based on two regimes, namely *below rated* and *rated*. In below rated conditions, blades lie at the optimal pitch angle, while the generator torque is scheduled with the rotor speed Ω to ensure that the tip speed ratio λ yields the maximum C_P. The rated condition occurs when Ω exceeds its rated value Ω_R. In this case, torque is fixed while pitch angle increases from its optimal value to limit the power output to P_R. Turbines can track a given power demand P_D (where $P_D \leq P_R$) by adjusting Ω_R and by setting $Q_R = P_D/\Omega_R$.

In this control strategy, the blade pitch angle θ serves as an indicator of the operating reserve – or margin – for a curtailed wind turbine (Tamaro and Bottasso, 2023). Typically, larger values of θ suggest a greater margin, as the turbine is functioning

below its optimal power coefficient. The minimum (so called "fine") value for θ corresponds to the optimal pitch angle θ_{opt}, which achieves the maximum C_P.

This controller was selected here because it directly accepts a power demand input and uses the blade pitch angle to accu-
170 rately follow it. Alternative control strategies could also be implemented, though they might lead to different APC performance.

2.4 Identification and treatment of saturation conditions

Saturations are detected on one turbine when the blade pitch lies at its optimal value plus a tolerance, and the tracking error exceeds a given threshold as specified in Sect. 3.1. When a wind turbine enters saturation, its power demand is set to $P^*_{D,i}$, which is the last value recorded before saturation, and its power share is computed as

175
$$\alpha_i = \frac{P_i}{P_{\mathrm{ref}} + P^{PI}_{\mathrm{ref}}}. \tag{7}$$

Then, its local tracking error is equally redistributed to non-saturated turbines in the form of an additional power demand, to ensure that $\sum_{i=1}^{N} \alpha_i = 1$. Notice that local isolated persistent saturation events do not necessarily introduce significant tracking errors as long as other turbines have enough margin to compensate.

Clearly, conditions in which all wind turbines are close to saturation are particularly harmful to the tracking accuracy, as a
180 cascading effect can be triggered that may lead to all turbines being saturated. In this case, all wind turbines operate in greedy mode, and if the TSO demand drops, a large negative Δ_P will result. To avoid this situation, when the wind farm produces more than the instantaneous demand (with a threshold, as explained earlier), every saturation condition is forcibly reset.

3 Methods

3.1 Experimental set-up

185 The wind tunnel experimental campaign is performed with a cluster of three G1 wind turbines (Bottasso and Campagnolo, 2022; Wang et al., 2021), labeled WT$_1$ (upstream), WT$_2$ (center), and WT$_3$ (downstream). The G1 scaled machine has a diameter D of 1.1 m, a rated rotor speed Ω_R of 850 RPM, a rated power P_R of 46 W, an optimal collective blade pitch angle θ_{OPT} of $0.43°$, and zero tilt. The time compression ratio is equal to about 80, which means that time flows much faster in the experiment than at full scale (Canet et al., 2021; Bottasso and Campagnolo, 2022). Each G1 is real-time controlled by a
190 dedicated Bachmann M1 PLC (Bachmann electronic GmbH, 2017), which executes the turbine-level controller described in Sect. 2.3 every $\Delta t = 4$ ms. The maximum yaw rate is equal to $20°\mathrm{s}^{-1}$, corresponding to approximately $0.25°\mathrm{s}^{-1}$ at full scale.

Tests are performed in the atmospheric test section of the wind tunnel of the Politecnico di Milano (Bottasso et al., 2014) in moderate turbulence conditions, with a power-law shear exponent $k = 0.14$, a TI $I = 6\%$ at hub height, and an integral length scale of turbulence of $0.79D$. The blockage ratio considering one G1 rotor is 1.8%, which is significantly smaller than previous
195 APC wind tunnel studies (Petrović et al., 2018; Gonzalez Silva et al., 2024). The three turbines are installed on a large turntable at a distance of five rotor diameters ($5D$) from each other. The rotational speed of the wind tunnel fans is kept constant during

the experiments. The resulting wind speed U_∞, measured by a Pitot tube placed $4D$ upstream of WT$_1$, is approximately equal to 5.5 ms^{-1}.

Two sets of experiments are conducted, respectively referred to in the following as "static" and "dynamic".

200   In the static tests, the turntable is fixed at an angle ψ to reproduce a specific wind direction. Two angles are considered, corresponding to partial rotor overlaps of 75% ($\psi = 2.8°$) and 50% ($\psi = 5.7°$), respectively. We define rotor overlap as the fraction (in percentage) of the diameter that two wind turbine rotors share when looking downstream. An overlap of 100% corresponds to perfectly aligned rotors (center-to-center), while 50% overlap means that the downstream rotor is laterally displaced by half a rotor diameter. In the static wind direction scenarios, each test has a duration of approximately 30 seconds,

205   corresponding to about 4 hours at full scale. Six repetitions are performed to reduce the uncertainties caused by the turbulent fluctuations of the flow.

In the dynamic tests, the turntable is rotated according to a pre-determined time series, in order to dynamically vary the wind direction over the cluster of turbines. In this case, each test has a duration of 180 seconds, to match the overall duration of the static tests.

210   Figure 2 shows the wind tunnel setup, while Fig. 3 shows the vertical profiles of the mean streamwise velocity and turbulence intensity measured at the location of the upstream turbine WT$_1$ for $\psi = 0°$.
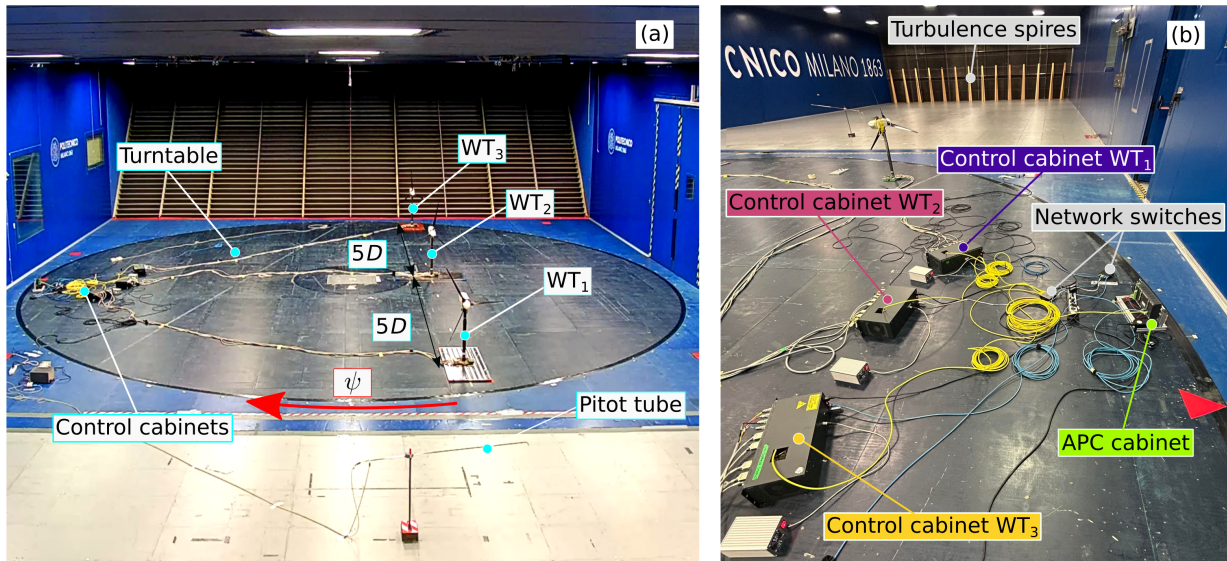
Figure 2. Wind tunnel setup **(a)** and closeup view of the control cabinets **(b)**.

The APC algorithms are implemented in MATLAB SIMULINK (The MathWorks, Inc., 2022), from which C++ codes are exported, and later compiled and loaded onto a Bachmann M1 PLC (Bachmann electronic GmbH, 2017). At every time step, the APC controller receives information on the current power demand and, for each wind turbine, on its instantaneous power

215   production, blade pitch angle, and tower base fore-aft bending moment. Furthermore, the APC controller is also informed in
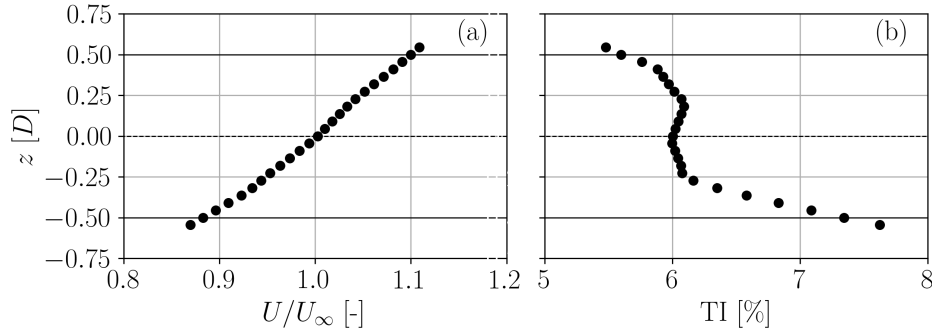
Figure 3. Wind tunnel inflow. Vertical wind speed profile **(a)**; vertical TI profile **(b)**.

real-time about the current wind farm power demand P_{ref} and the current wind direction ψ. Within one sampling period, the setpoints of demanded power and nacelle yaw are computed by the APC controller and dispatched to each wind turbine. The direction of the wind relative to the farm is read from the turntable encoder. Therefore, its measurement can be considered exact up to the accuracy of this sensor. In the field, the knowledge of ψ is definitively more uncertain, due to the typically limited

220 accuracy of the onboard anemometry system and the yaw encoder. The effects of wind direction uncertainties on wake steering performance were experimentally investigated by Campagnolo et al. (2020), using a very similar setup as the one considered here.

The control cabinets executing the wind turbine and APC controllers are connected to a PC in the control room via Ethernet. This PC is used to monitor the wind turbine sensors through a graphical user interface, to install and uninstall applications,

225 to activate the wind farm controller, and to modify its settings as necessary. The Modbus communication protocol is used to start simultaneous data acquisitions, due to its compatibility with MATLAB. Communication between the APC and the wind turbine controllers is instead accomplished with Ethernet cables through the Profinet protocol (Profibus Nutzerorganisation e. V. (PNO), 2018). This system was chosen due to its relatively fast communication capabilities and integration with the existing setup. The APC algorithms are executed with a timestep of 4 ms (equivalent to approximately 0.3 s at full scale) to match

230 the timestep of the wind turbine controllers. In CL+MR, the open-loop scheduler is updated 100 times faster, i.e. every 0.4 s, corresponding to approximately 30 s at full scale. A sketch of the connections among the various components of the system is shown in Fig. 4.

Local saturation conditions are indicated by a flag that is raised when both of the following conditions are simultaneously verified:

235   – the tracking error of a turbine exceeds 1% of the rated power P_R, i.e. 0.46 W, and

   – its blade pitch angle is lower than $\theta_{\mathrm{OPT}} = 0.37°$.

Saturation conditions are also used to control the integral part of the APC PI controller. As discussed in Sect. 2.1.2, the integrator in the APC loop includes an anti-windup element that is activated when all turbines in the wind farm become saturated. This mechanism quickly reduces the integral term by applying to it a gain of 0.99 at each timestep.
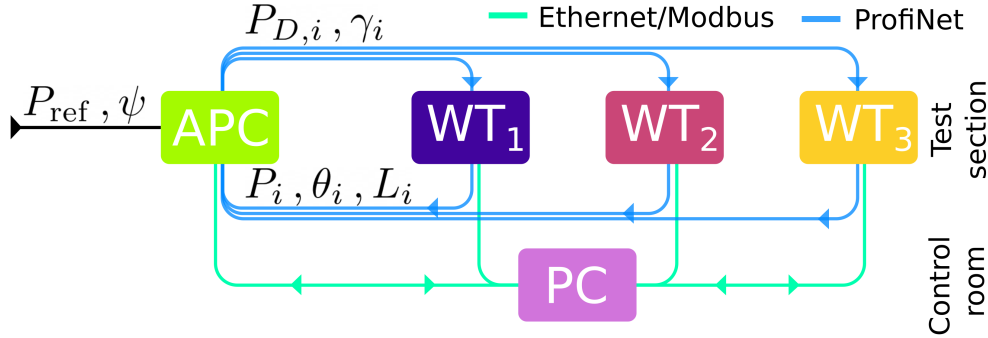
Figure 4. Sketch of the wiring connections among wind turbines, APC, and PC.

All saturation flags are reset when the wind farm power output exceeds P_{ref} by more than $3\%P_R = 1.38$ W. This mechanism addresses the situation in which all turbines become saturated. In such cases, the rotors are commanded to follow $P_{D,i} = P_{D,i}^*$, i.e. the last demanded power value prior to saturation, as described in Sect. 2.4. However, when all turbines are saturated, the system is unable to detect changes in P_{ref}. Consequently, the machines would continue tracking $P_{D,i}^*$ even if P_{ref} decreases. To avoid this situation, the APC integrator and all saturations are reset whenever $\Delta_P < -3\%P_R$. In the CLD PI controller, the integrator is reset either when all turbines become saturated or when this condition ends.

For all controllers described in Sect. 2, the power generated by each turbine is low-pass filtered using a first-order transfer function with a cut-off frequency of 5 Hz ($= 0.35\,\Omega_R$), before inputing it in the farm-level controller. A first-order filter is chosen here to limit the time delay associated with higher-order filters, which would hinder tracking accuracy. A cut-off frequency of 1.57 Hz ($= 0.11,\Omega_R$) is used to update the power setpoints, while a lower cut-off of 0.72 Hz ($= 0.05\,\Omega_R$) is employed for the power demand. These different cut-off frequencies are selected to ensure that the power demand signal remains smooth while minimizing delay in the setpoints.

For CL+LB, fore-aft bending moments are filtered using a moving average with a fundamental frequency of 1 Hz ($= 0.07\,\Omega_R$).

3.2 Turntable control

The wind tunnel turntable has a diameter of 13 m, and it can be rotated to follow a prescribed time history (Campagnolo et al., 2020). Figure 5 shows the direction time history $\psi(t)$, which is scaled (Campagnolo et al., 2020) from an onshore test site in northern Germany (Bromm et al., 2018).

Throughout the experiment, the wind direction changes sign five times. This condition is particularly challenging when performing double-sided wake steering since it requires a sudden, large yaw angle variation to change the side where wakes are deflected.

Figure 6a presents the measured available farm power as a function of wind direction ψ, while Fig. 6b shows the measured variation of local power share as a function of ψ in the absence of wind farm control (i.e. in standard greedy mode).
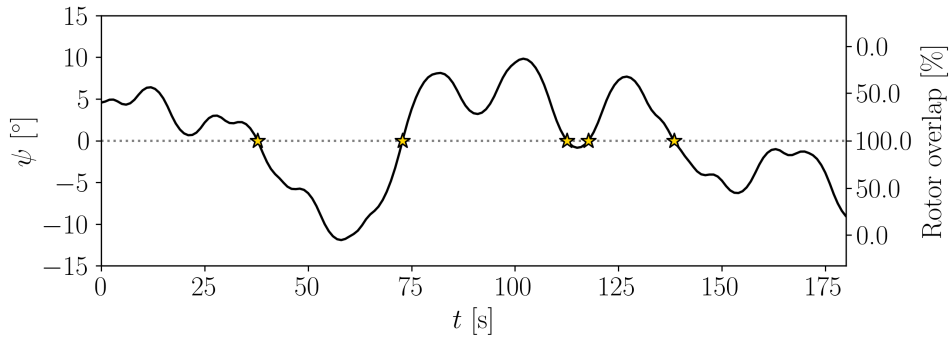
Figure 5. Time history of wind direction $\psi(t)$. Full rotor alignments ($\psi = 0°$) are highlighted.
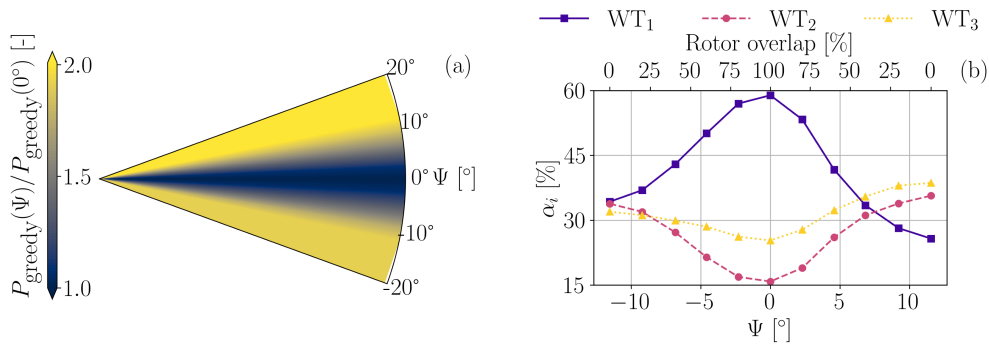
Figure 6. **(a)** Non-dimensional available power $P_{\text{greedy}}(\psi)/P_{\text{greedy}}(0°)$ as a function of wind direction ψ. **(b)** Local power setpoints as functions of ψ in greedy mode. When $\psi = 0°$, the wind turbines are fully aligned.

Figure 6a highlights the strong effect of wake impingement on power production. The minimum available power is visible in correspondence with $\psi \approx 0°$. The lack of symmetry with respect to ψ is due to a lateral inhomogeneity of the flow within

265 the wind tunnel (Campagnolo et al., 2020). Overall, WT$_2$ appears to be suffering the most significant power losses, as in fact it produces only 15% of the wind farm power when $\psi = 0°$. WT$_3$ presents a slightly higher power due to the high turbulence in the two wakes that impinge on it, which speeds up their recovery.

3.3 Reference power demand signal

A dynamic reference power signal typical of automatic generation control (AGC) is used as input signal to the farm-level

270 tracking controllers. AGC is the secondary response regime of grid frequency control, and it consists of dynamically adjusting the power output of a plant according to the request of the TSO (Aho et al., 2012). A similar signal has been considered by other authors (Fleming et al., 2016; van Wingerden et al., 2017; Vali et al., 2019; Shapiro et al., 2017; Boersma et al., 2018).

The signal is defined as

$$P(t, \psi) = P_{\text{greedy}}(\psi) \left(b + c n_k^{\text{AGC}}(t) \right), \tag{8}$$

275 where $n_k^{\text{AGC}}(t)$ is a normalized time-dependent test signal, $P_{\text{greedy}}(\psi)$ is the available power of the wind farm in greedy aligned conditions at a specific wind direction ψ, and b and c are two parameters that respectively shift and scale n_k^{AGC}.

Due to the small size of the models, the original signal is accelerated in time by a factor of 81.73 (Bottasso and Campagnolo, 2022). Figure 7a shows n_k^{AGC} as a function of time. In the tests with the dynamic turntable, the reference power signal in Fig. 7a is looped multiple times for a total length of three minutes. In this case, the instantaneous available wind farm

280 power $P_{\text{greedy}}(\psi)$ depends on the instantaneous wind direction ψ as shown in Fig. 6a. Figure 7b shows the time history of $n_k^{\text{AGC}}(t) P_{\text{greedy}}(\psi)/P_{\text{greedy}}(0°)$, where both the full-scale (top x axis) and wind tunnel (bottom x axis) time scales are reported.
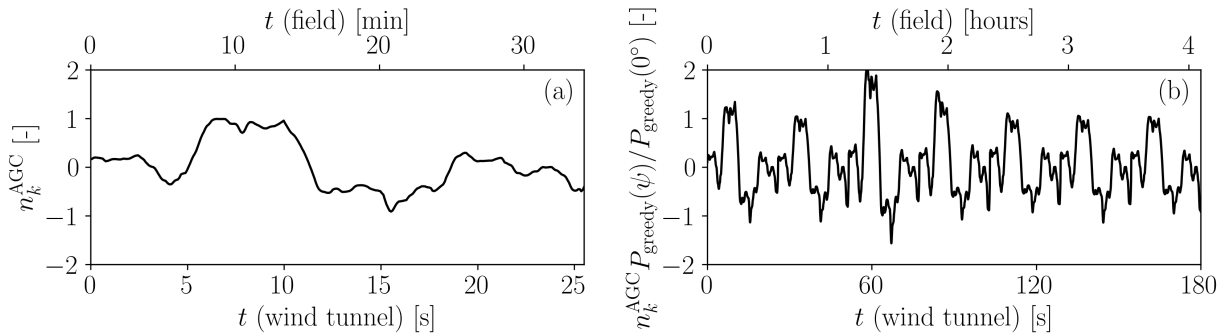
Figure 7. Time series of the reference test signal n_k^{AGC} **(a)**, and of the normalized power reference used in the dynamic turntable experiments **(b)**. The additional x axis on the top part of the plot indicates full-scale time.

The reference power signal is initialized with a rising ramp to reduce the effects of initial transients. Notice how a 4-hour-long test in the field is replicated in the significantly shorter time of 180 seconds in the wind tunnel. It is important to notice

285 that the test time of 3 minutes covers 24 full-scale 10-minute turbulent realizations, which ensures the statistical convergence of results (Liew and Larsen, 2022).

3.4 Tuning procedure of the PI gains

The gains used in the APC controllers are tuned using a digital twin of the wind tunnel setup. This model of the experiment is implemented in SIMULINK (The MathWorks, Inc., 2022) and includes three blocks representing the wind turbines, each

290 running the same controller used in the wind tunnel tests. The drivetrain dynamics are modeled as described in Campagnolo et al. (2022a), while rotor aerodynamics are represented using LUTs computed offline with a blade element momentum (BEM) model of the G1 (Wang et al., 2020). The LUTs schedule rotor thrust and torque as functions of turbine operating conditions. Tower dynamics are modeled with a second-order system.

The Jensen wake model (Jensen, 1983), combined with the instantaneous thrust coefficient C_T, is used to estimate the wake deficit for downstream turbines. A delay is used to simulate the time required for wake effects to propagate downstream. The same CL and CL+LB controllers used in the wind tunnel experiments are included in the digital twin. To improve the robustness of gain tuning, zero-mean white noise with a variance of $0.25\,\mathrm{W}^2$ is added to the measured input power.

Gain optimization is performed with the goal of reducing the influence of saturation events, using a gradient-based interior-point algorithm with a power demand signal characterized by $P_{\mathrm{greedy}} = 55\,\mathrm{W}$, $b = 0.8$, and $c = 0.1$.

For the CL+LB controller, the cost function is defined as

$$J = 0.75\,\overline{\Delta}_P + 0.25 \sum_{i=1}^{N} \overline{\Delta}_{L,i}, \tag{9}$$

which represents a weighted sum of the non-dimensional tracking error $\overline{\Delta}_P$ and the non-dimensional load-balancing error $\overline{\Delta}_{L,i}$. Both quantities are scaled to lie in the interval $[0,1]$.

The resulting gains for the APC loop are

$$K_{\mathrm{APC}}^P = 1.3127 \quad [-], \qquad K_{\mathrm{APC}}^I = 14.9253\,\mathrm{s}^{-1} = 1.05\,\Omega_R.$$

For the CLD loop, the gains are

$$K_{\mathrm{CLD}}^P = 0.03427\,\mathrm{Nm}^{-1} = 0.52\,L_R^{-1}, \qquad K_{\mathrm{CLD}}^I = 0.07959\,\mathrm{Nm}^{-1}\mathrm{s}^{-1} = 0.09\,L_R^{-1}\Omega_R,$$

where $L_R = 15.2\,\mathrm{Nm}$ is the tower base fore-aft bending moment of the G1 turbine at rated wind speed.

4 Steady-state model

The engineering farm flow model FLORIS v3 (National Renewable Energy Laboratory, 2022) is used here both to synthesize the open-loop part of the controller and to perform steady-state analyses. The wake deficit and deflection models proposed by Bastankhah and Porté-Agel (2014) are employed, along with the turbulence model by Crespo and Hernàndez (1996). In both cases, the model parameters are fine-tuned to replicate wind tunnel conditions, as summarized in Appendix A.

FLORIS is also augmented with a heterogeneous wind map that replicates the asymmetric inflow of the wind tunnel shown in Sect. 3.2 (Campagnolo et al., 2022b), following the procedure proposed by von Braunbehrens et al. (2023). In OL and CL, the same engineering flow model is used to assign the power share setpoints α_i as functions of ψ, given the ambient conditions of the experiments.

4.1 Setpoints for CL+MR: combining wake steering with off-rated operation

In CL+MR, wind turbines are subjected to induction control and simultaneously perform wake steering. To model this combined off-rated and misaligned operation, LUTs of power coefficient C_P and thrust coefficient C_T are computed via an analytical model (Tamaro et al., 2024a). The adoption of such a model is motivated by the fact that off-rated operation spans a wide range of C_T values – and misaligned operation is strongly dependent on C_T (Cossu, 2021; Heck et al., 2023).

Another important aspect typical of scaled wind turbine models is the effect of the chord-based Reynolds number on the aerodynamic performance of the rotor (Bottasso and Campagnolo, 2022). This is relevant since with the controller described in

325 Sect. 2.3, turbines operating in off-rated conditions experience low rotational speeds. These effects were taken into account by using a BEM model of the G1 that includes a dependency on the chord-based Reynolds number (Wang et al., 2020). Figures 8 and 9 show examples of LUTs for C_P and C_T, where the auxiliary factor ϵ has been introduced to quantify the level of derating, with $\epsilon = 1$ corresponding to the greedy power mode.
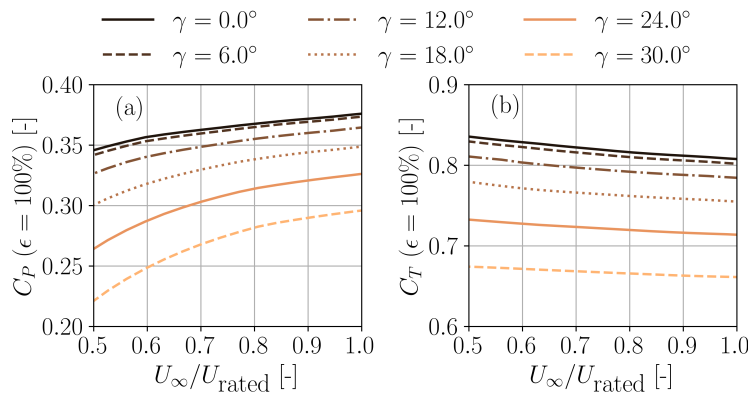
Figure 8. LUTs for **(a)** power coefficient C_P and **(b)** thrust coefficient C_T as functions of wind speed for the G1 turbine. Results corresponds to a power scaling factor $\epsilon = 100\%$, (i.e. no curtailment), and different yaw angles γ.
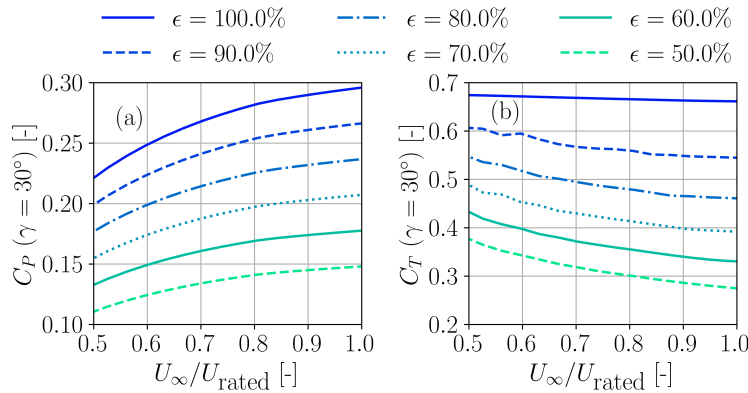
Figure 9. LUTs for **(a)** power coefficient C_P and **(b)** thrust coefficient C_T as functions of wind speed for the G1 turbine. Results correspond to a yaw angle $\gamma = 30°$ and different power scaling factors ϵ, representing the level of power curtailment.

Since both power demand and wind direction vary, the LUTs for $\gamma_i(P_D, \psi)$ and $\alpha_i(P_D, \psi)$ are two-dimensional. Other

330 model inputs, such as TI and inflow shear, are fixed as described in Sect. 3.1. To generate the LUTs, different optimizations are solved for each wind direction and wind farm power demand. When the optimization converges, the resulting power share

setpoints are computed as $\alpha_i = P_i / \sum_{i=1}^{N} P_i$, and they are stored together with the yaw setpoints. The optimization problem is solved with the gradient-based Sequential Quadratic Programming (SQP) method (Brayton et al., 1979). Results are shown in Figs. 10 and 11 for the yaw and power setpoints, respectively.
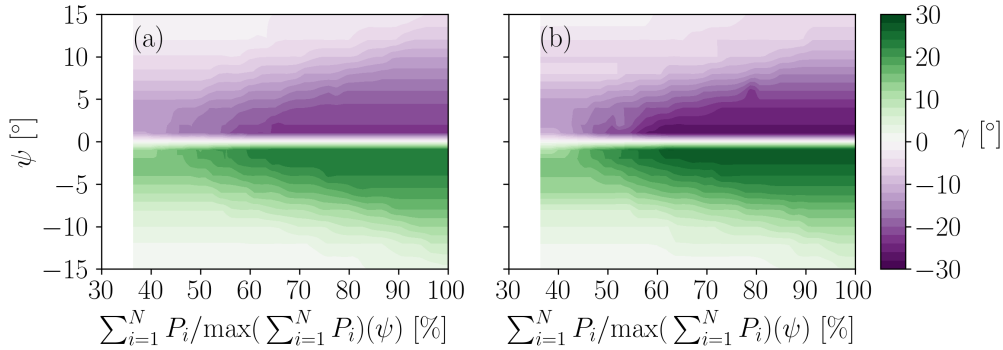
Figure 10. Optimal yaw setpoints γ that maximize the minimum power reserve for the experimental setup, plotted against the power demanded to the wind farm in percentage of the maximum power, and the inflow wind direction ψ. **(a)** WT$_1$; **(b)** WT$_2$.
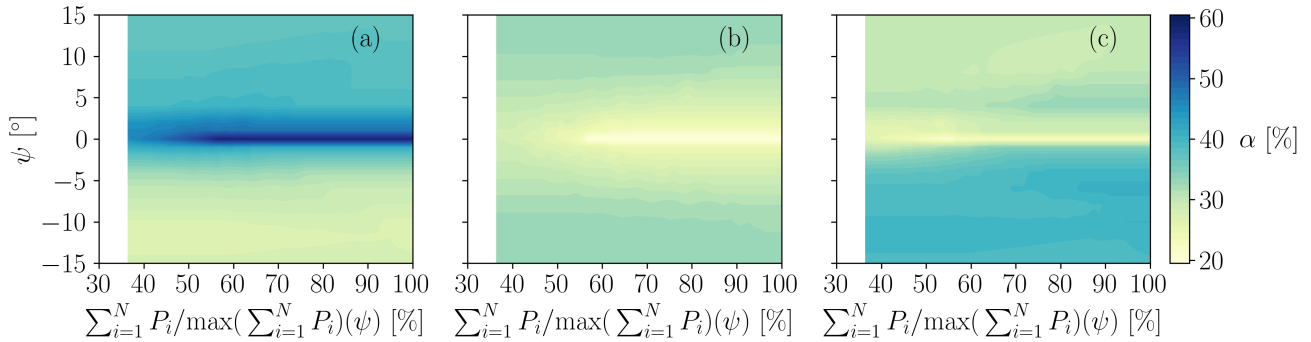
Figure 11. Optimal power setpoints α that maximize the minimum power reserve for the experimental setup, plotted against the power demanded to the wind farm in percentage of the maximum power, and the inflow wind direction ψ. **(a)** WT$_1$; **(b)** WT$_2$; **(c)** WT$_3$.

335   In the figures, $\psi = 0°$ represents a condition of precise alignment and therefore full wake impingement. Conversely, when $0° < |\psi| \leq 11.3°$, partial wake impingement occurs. The yaw setpoints present, in fact, a maximum absolute value in full waking, where steering is heavily used to increase power reserves. As ψ increases, the power setpoints start converging towards an equal power dispatch, i.e. $\alpha_i = 1/N$, while the yaw misalignment is progressively reduced. In fact, as ψ deviates away from $0°$, wake impingement is less prominent, and all turbines perceive similar local inflow conditions.

340   The treatment of the $\psi = 0°$ condition is particularly relevant: under dynamic wind direction variations, when ψ switches sign, the upstream wind turbines must change their yaw setpoint by more than $\pm 40°$. Delays in following this demand – which are expected due to the necessarily limited speed of the yaw actuation system – could result in relevant power losses, since the

wake may be temporarily deflected towards downstream rotors, instead of away from them. To avoid this situation, no optimal
wake steering is performed between $-2° < \psi < 2°$, but instead, the setpoints are interpolated from the values at $\pm 2°$ to ensure

345 a smooth transition when ψ switches sign. This solution should not result in a hindrance to the overall effectiveness of wake
steering, since deflecting wakes is more effective in partial than in full impingement (Howland et al., 2019).

During operation, α_i and γ_i are linearly interpolated from the LUTs in Figs. 10 and 11 based on the average power demand
and wind direction computed over the previous 0.4 seconds. Clipping to the last available value of the LUT is used to avoid
extrapolating.

350 **4.2 Estimation of the power margins**

The power reserves for CL + MR are compared to those of OL in steady-state conditions, using the simulation environment
described earlier. The comparison considers the difference between the power produced P_i and the available power $P_{a,i}$ for
each turbine. Figure 12 shows the locally available power and the minimum power (last column) in the farm for two wind
directions, i.e. $\psi = 2.8°$ and $5.7°$, corresponding to partial rotor overlaps of 75% and 50%, respectively.
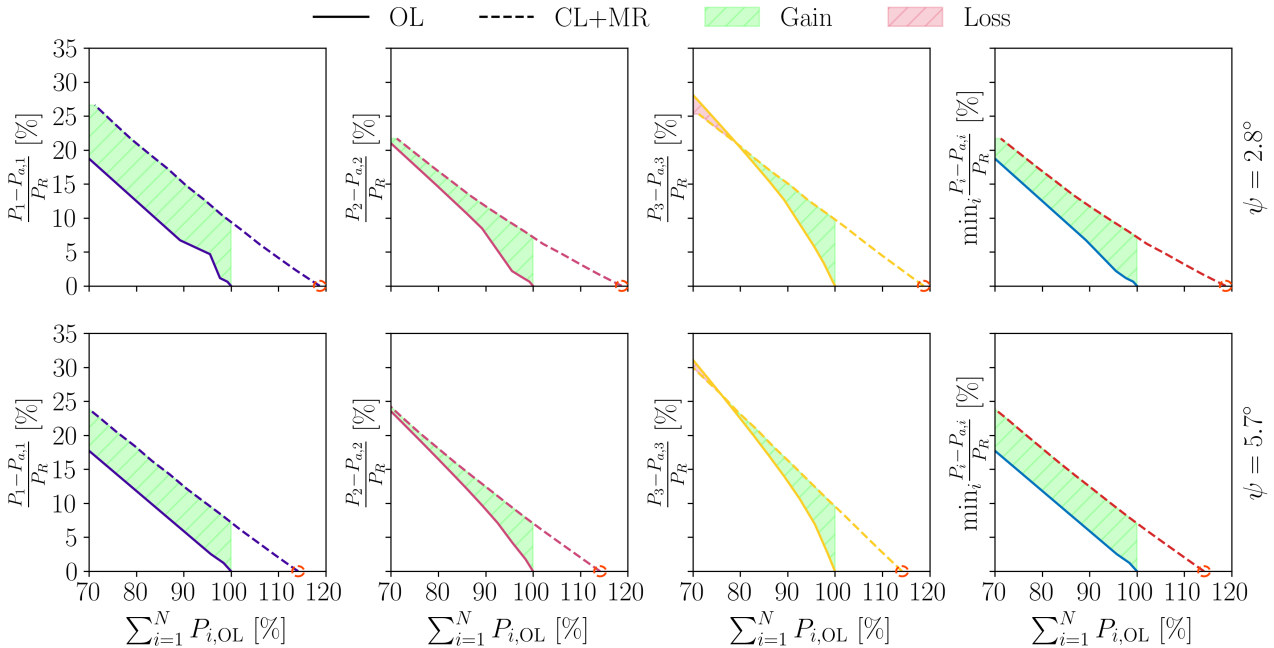
Figure 12. Locally available power normalized with the rated power P_R, obtained with a purely inductive wind farm control (labeled OL),
and with the maximum-reserve strategy (labeled CL+MR) for $\psi = 2.8°$ and $\psi = 5.7°$. **(a)** WT$_1$; **(b)** WT$_2$; **(c)** WT$_3$; **(d)** minimum value in
the wind farm. On the x axis, the wind farm power is normalized with its maximum value without wake steering. Red circles indicate the
classical maximum power solution.

Results show that the largest wind farm power gain is obtained for $\psi = 2.8°$ ($\approx +18\%$), followed by $\psi = 5.7°$ ($\approx +14\%$),
confirming that wake steering is particularly beneficial in partial wake impingement conditions (Howland et al., 2019). As a
result of the higher wind farm power, a significant gain in power reserve is achieved with CL+MR relative to OL, in particular
for the front turbine WT$_1$. This is favorable, since WT$_1$ is often required to compensate for the saturations that may affect waked
rotors. For these downstream turbines, the benefit of CL+MR becomes evident at severe power demands, i.e. $\sum_{i=1}^{N} P_{i,\mathrm{OL}} \approx$
95%, and it gradually decreases as $\sum_i P_{i,\mathrm{OL}}$ is reduced because of the loss of effectiveness of wake steering due to the lower
operational C_T of upstream rotors. This, in fact, implies a lower velocity deficit in the wake and a less prominent deflection.
Overall, CL+MR yields a distribution of power reserves across the turbines that is more uniform than when using the OL
method, consistently with the goal of the optimization.

5 Static wind direction experiments

In this section, we present the wind tunnel results for two fixed wind direction values equal to $\psi = 2.8°$ and $5.7°$, corresponding
to partial rotor overlaps of 75% and 50%, respectively.

5.1 Power tracking accuracy

5.1.1 Wind farm tracking errors

Figures 13 and 14 present the root mean square (RMS) of the power tracking error recorded at the three power request levels
$b = 0.8, 0.85, 0.9$, by each APC algorithm in the wind tunnel experiments. For each controller, six measurements are shown,
indicating six repetitions, and whiskers indicate the mean RMS error and its uncertainty considering a 95% confidence level.
Figure 13 presents the RMS of tracking error obtained for $\psi = 2.8°$, while Fig. 14 refers to the case $\psi = 5.7°$.
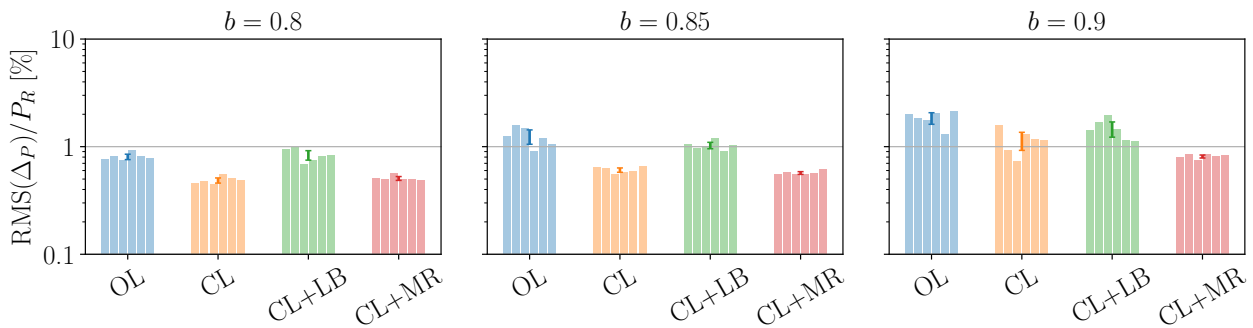
Figure 13. RMS of wind farm power tracking errors measured for the four APC algorithms and three power demand levels b. Static experiment with fixed wind direction $\psi = 2.8°$, corresponding to 75% rotor overlap. The results from six repetitions are reported with bars for each APC algorithm and power demand. Whiskers indicate 95% confidence intervals.
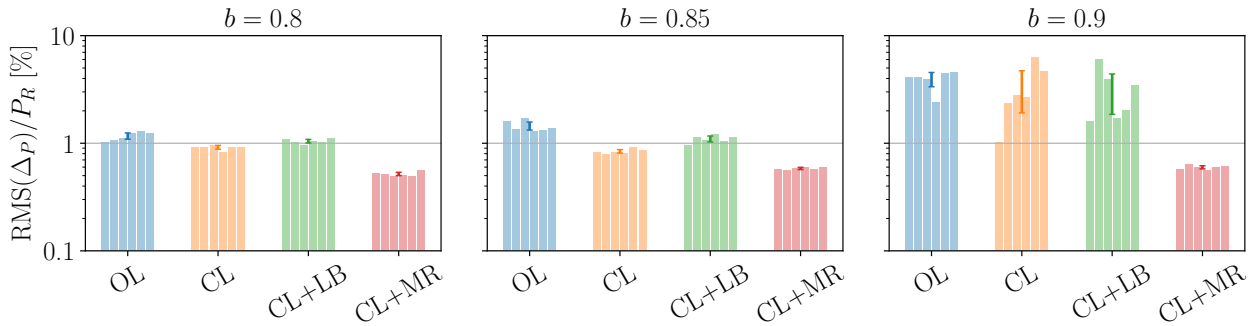
Figure 14. RMS of wind farm power tracking errors measured for the four APC algorithms and three power demand levels b. Static experiment with fixed wind direction $\psi = 5.7°$, corresponding to 50% rotor overlap. The results from six repetitions are reported with bars for each APC algorithm and power demand. Whiskers indicate 95% confidence intervals.

The plots show that the tracking error grows with the power request determined by parameter b. Closed-loop methods reduce the tracking error consistently, with a generally larger effectiveness for $\psi = 2.8°$, i.e. for the higher rotor overlap case. Interestingly, the variability of the results increases significantly as parameter b grows in all cases except for CL+MR. The smaller variability observed for CL+MR is likely due to larger power reserves, which reduce the likelihood of simultaneous saturation events that can dramatically affect tracking accuracy.

5.1.2 Wind turbine tracking errors

Figures 15 and 16 show the tracking RMS error of each wind turbine for various power demand levels, for $\psi = 2.8°$ and $\psi = 5.7°$, respectively.

In the OL and CL+LB cases, waked rotors present the highest tracking error. In both cases, this is due to the generally low power reserves of waked rotors, which is exacerbated by the lack of a closed-loop for OL and by the coordinated load distribution for CL+LB. Compared to OL, CL increases the tracking errors of WT$_1$ because it calls this front turbine operating in freestream to compensate for the saturation of the waked turbines further downstream. CL+MR presents a consistently balanced error distribution. This is likely due to the rather uniform distribution of power reserves, which implies that all turbines have a similar likelihood of not being able to follow a local demand.

It should be remarked that for all methods except for OL, a saturated turbine will experience significant tracking errors. This does not necessarily imply a low wind farm tracking accuracy, but only as long as other turbines are able compensate. Therefore, it is important to ensure that local power reserves are not exhausted, which is precisely what the maximum-reserve formulation tries to accomplish.
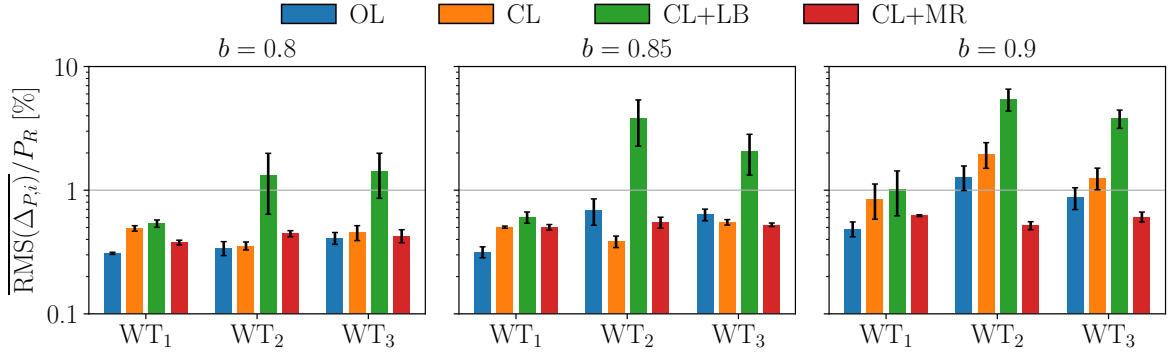
Figure 15. RMS of local power tracking errors for the four APC algorithms and three power demand levels b. Static experiment with fixed wind direction $\psi = 2.8°$, corresponding to 75% rotor overlap. Whiskers indicate 95% confidence intervals.
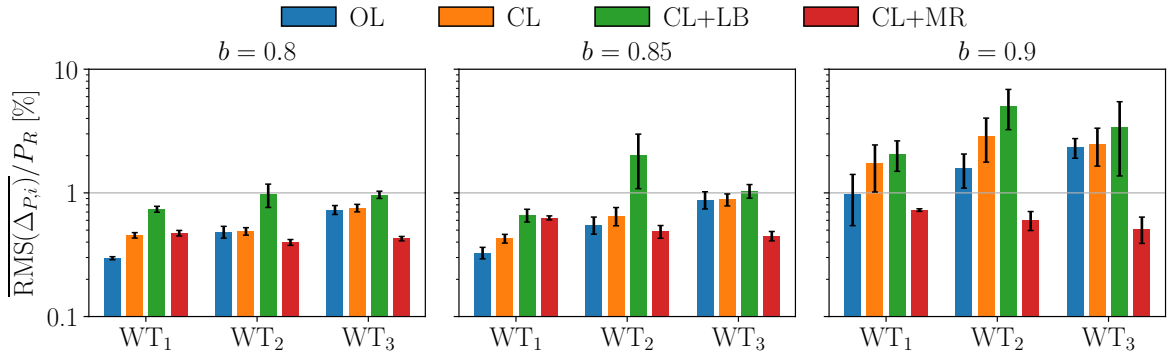
Figure 16. RMS of local power tracking errors for the four APC algorithms and three power demand levels b. Static experiment with fixed wind direction $\psi = 5.7°$, corresponding to 50% rotor overlap. Whiskers indicate 95% confidence intervals.

5.2 Power reserve distribution

To quantify the mean power reserve of each turbine, we analyze the average collective blade pitch angle $\overline{\theta}$. With the controller described in Sect. 2.3, the closer $\overline{\theta}$ is to the optimal pitch θ_{OPT}, the less power reserve is available. Figures 17 and 18 show the local mean collective blade pitch angle for $\psi = 2.8°$ and $\psi = 5.7°$, respectively.

395   Consistently with the tracking error analysis, $\overline{\theta}$ appears to decrease as the power demand increases. OL and CL+LB present a power reserve distribution that is significantly unbalanced towards WT_1. In particular, CL+LB presents the highest values of $\overline{\theta}$ for WT_1, but at the same time it also always yields low values of $\overline{\theta}$ for waked rotors. CL remarkably improves the balancing of power reserves compared to OL, especially for $\psi = 2.8°$ and for low values of b. CL+MR presents a rather uniform distribution
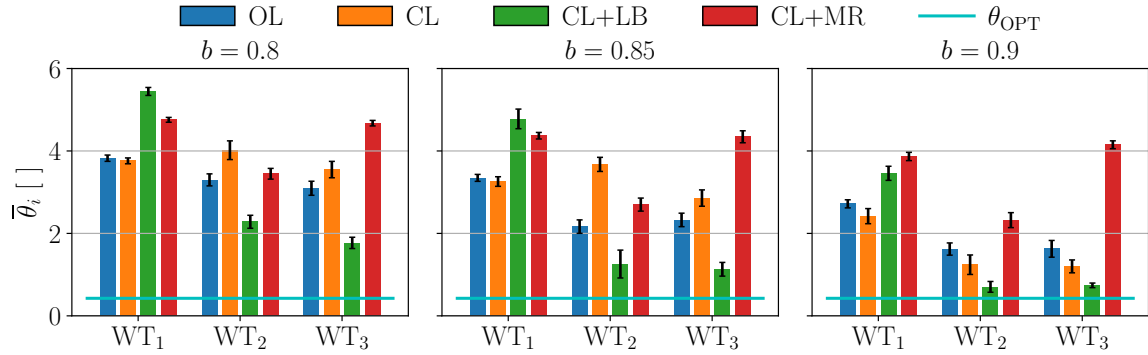
Figure 17. Local average blade pitch angle $\overline{\theta}$ from the static turntable experiment for wind direction $\psi = 2.8°$, corresponding to a 75% rotor overlap. Whiskers indicate 95% confidence intervals. Results are presented for three power demand levels b.
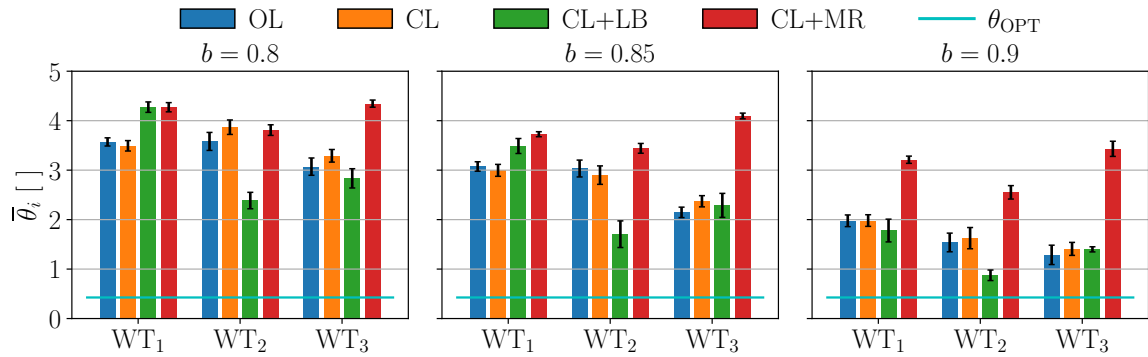
Figure 18. Local average blade pitch angle $\overline{\theta}$ from the static turntable experiment with wind direction $\psi = 5.7°$, corresponding to a 50% rotor overlap. Whiskers indicate 95% confidence intervals. Results are presented for three power demand levels b.

of the power reserves, favoring especially the most waked rotor, i.e. WT_3. This directly confirms the effectiveness of wake

400   steering, which, by laterally moving upstream wakes, improves the power reserve of the most downstream rotor.

5.3   Loads and fatigue

In the following loads and fatigue analysis, we only display data for the 75% rotor overlap scenario, since results for $\psi = 5.7°$ (50% rotor overlap) are similar (and reported, for completeness, in Appendix C).

The mean local load balancing error of each rotor is shown in Fig. 19.

405   Results show that for OL and CL, loading is maximum on WT_1 and decreases when moving downstream. CL+LB effectively balances loads in the wind farm, with remarkable effectiveness for $b < 0.9$. When $b = 0.9$, the significant increase in saturation
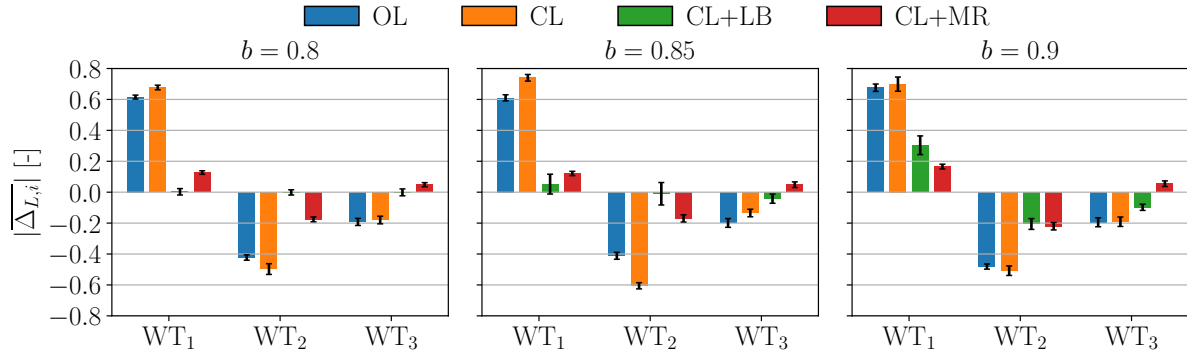
Figure 19. Mean local load balancing error for the tower-base fore-aft bending moment for the static turntable experiment with wind direction $\psi = 2.8°$, corresponding to a 75% rotor overlap. L is normalized by $\frac{1}{2}\rho U_\infty^2$. Positive values indicate loading above the wind farm average. Whiskers indicate the mean error over six repetitions and its uncertainty considering a 95% confidence level. Results are presented for three power demand levels b.

events is such that loads cannot be balanced anymore, since power tracking accuracy is prioritized. This shows the limit of the load balancing strategy that, in some cases, is unable to achieve the goals for which it has been formulated.

Next, damage equivalent loads (DELs) at tower base are presented in Fig. 20.
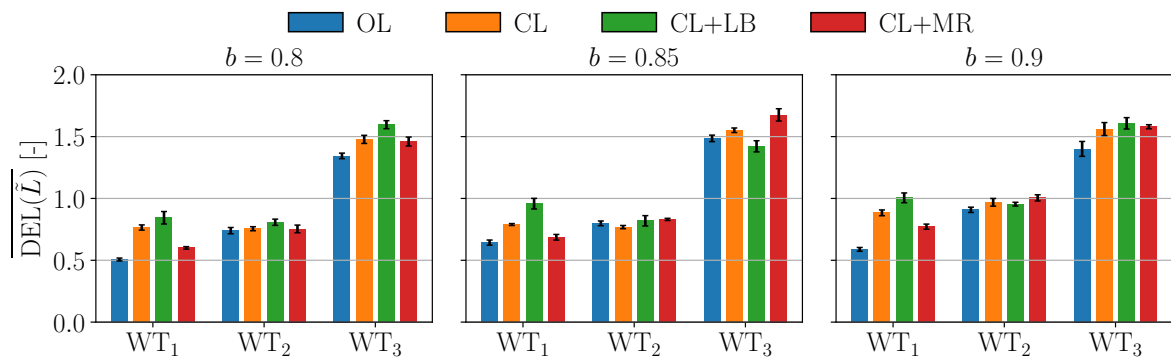
Figure 20. Normalized tower-base fore-aft DELs from the static turntable experiment for a wind direction $\psi = 2.8°$, corresponding to 75% rotor overlap. Whiskers indicate the mean DEL over six repetitions and its uncertainty considering a 95% confidence level. Results are presented for three power demand levels b.

410   Results show that waked turbines generally suffer more damage than those operating in freestream conditions, with WT_3 being consistently the most damaged. This is likely due to the highly turbulent local inflow and the partial wake impingement that introduce numerous load cycles on these machines. OL generally presents a rather low level of fatigue, which is due to the

limited pitch actuation deriving from the lack of a closed-loop correction. At the same time, CL+LB yields the highest damage for WT_1. In contrast to OL, this is caused by the more frequent blade pitch actuation that follows the occurrence of saturation

415 events happening downstream. CL+MR reduces the fatigue of WT_3 in almost all instances, because wake steering applied to WT_2 mitigates partial wake overlap effects. CL+MR also reduces the fatigue of WT_1, likely because fewer saturation events occur at downstream rotors, which WT_1 would otherwise have to compensate for through additional blade pitch activity. The analysis of blade pitch actuator duty cycle is reported in Appendix B.

6 Dynamic wind direction experiments

420 The time series of the experiments conducted while moving the turntable are shown in Fig. 21 for the power requests $b = 0.8$, $b = 0.85$, and $b = 0.9$. In the plots, the expected available wind farm power P_{greedy} is displayed in grey in the background. P_{greedy} has been obtained with the turbines operating in greedy mode and fully aligned with the inflow, as presented in Sect. 3.2.

From a first qualitative impression, all methods seem to follow the reference signal accurately. It is clear that OL and CL share the same power share setpoints α_i, since $P_{D,1}$, $P_{D,2}$ and $P_{D,3}$ are similar. In CL, however, some saturations can be seen,

425 for instance when $t \approx 100$ s and $b = 0.9$. CL+LB presents a very different distribution of power shares, and it appears that the individual power outputs $P_{D,i}$ of the three turbines are often similar, possibly to balance the loads in conditions of low wake impingement. The power share distribution of CL+MR resembles that of OL, although $P_{D,1}$ is generally lower and $P_{D,3}$ higher due to wake steering.

Overall, the plots clearly show that, as the power demand is increased, the power request P_{ref} approaches the greedy power,

430 and more saturation events arise, as indicated by the flat lines of $P_{D,i}$ in CL, CL+LB, and CL+MR.

In the zoomed windows of the plot, an example is highlighted where OL presents a significant deviation from P_{ref} at the wind farm level, because of a saturation of WT_2 lasting approximately 10 seconds. This same problem also occurs for CL. However, the wind farm tracking error is clearly reduced because WT_1 and WT_3 are able to compensate. Quite differently, CL+LB and CL+MR show excellent tracking performance in the same scenario. This similar performance is, however, achieved in different

435 ways: in CL+LB, both WT_2 and WT_3 are saturated and therefore operate in greedy mode, while WT_1 is fully responsible for tracking P_{ref}. In CL+MR, no saturation events are visible, which indicates generally larger power reserves for all turbines.

6.1 Power tracking accuracy

The RMS of the tracking error is shown in Fig. 22.

Consistently with the static wind direction results, OL shows the worst performance of all APC methods. At moderate power

440 demands, for $b \leq 0.85$, CL and CL+MR exhibit the best performance. For $b = 0.9$, CL+MR provides the lowest RMS Δ_P. The relative improvements achieved by CL+MR are less pronounced in the dynamic tests than in the static ones, as the effects of wake steering are less beneficial at large turntable misalignments where wake interactions are much reduced.
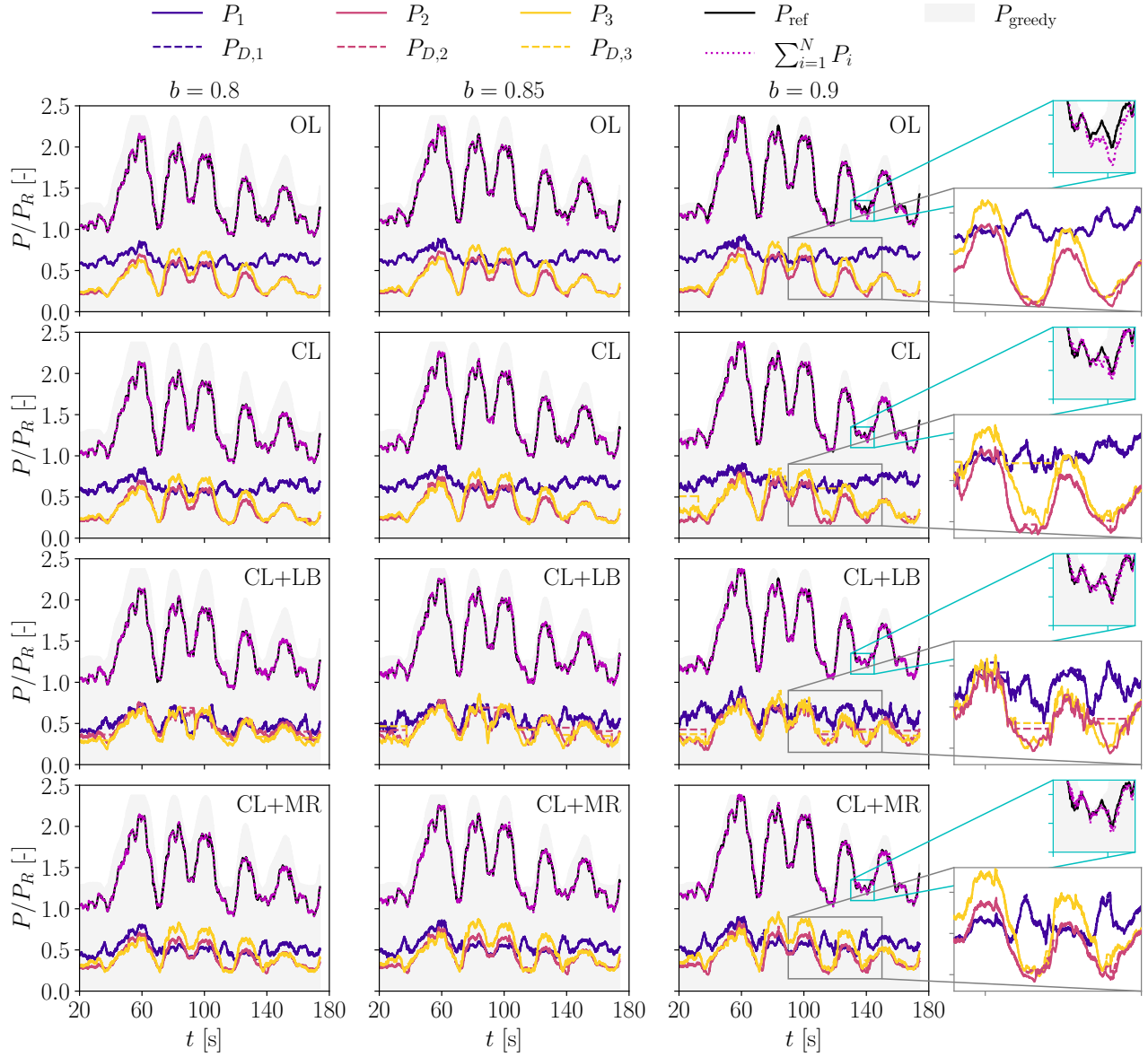
Figure 21. Time series of a power tracking experiment with dynamic wind direction variation, for the four APC algorithms and three power demand levels b. The expected available wind farm power in greedy mode – based on the instantaneous wind direction – is shown in the background in grey.
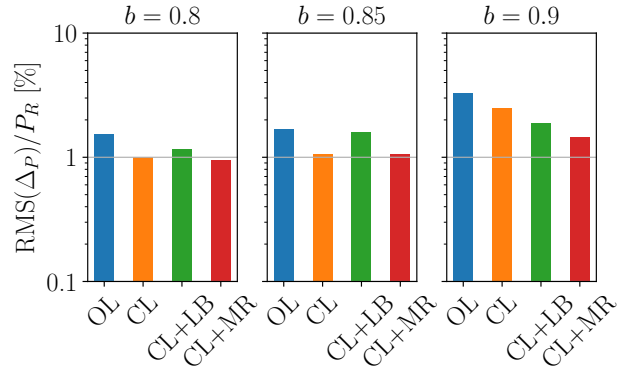
Figure 22. RMS of power tracking errors for the four APC algorithms and three power demand levels b. Experiment with dynamic wind direction variations.

Figure 23 shows how the errors are distributed across the three turbines. It is important to mention that saturated turbines will display extreme error values $\Delta_{P,i}$, although this does not necessarily imply a large wind farm tracking error Δ_P, since
445   (except than for OL) non-saturated rotors can compensate for their error.
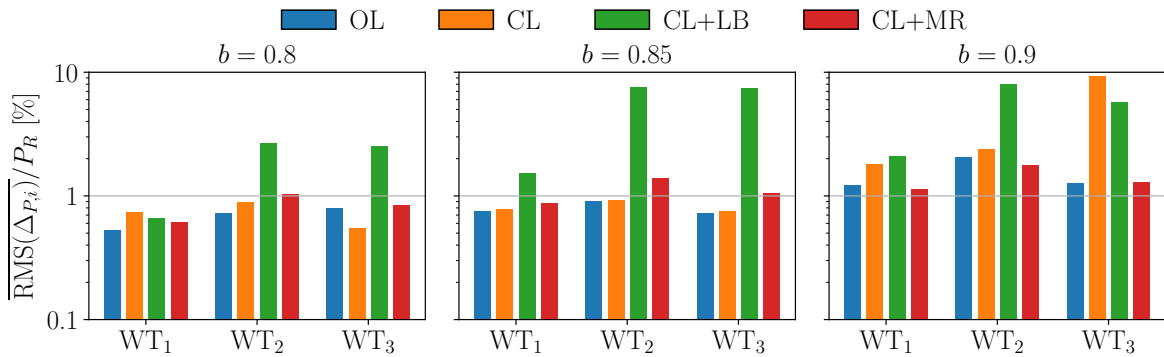
Figure 23. Local RMS of power tracking errors for the four APC algorithms and three power demand levels b. Experiment with dynamic wind direction variations.

The figure shows relatively large tracking errors for OL, because of a lack of feedback capable of handling saturation conditions. Significant tracking errors can be observed for waked rotors in the case CL+LB, indicating persistent saturations, as seen in the zoomed regions of Fig. 21.

Figure 24 supports this analysis by presenting the mean collective blade pitch angles of the turbines during the experiment.
450   As mentioned in the static direction study, $\overline{\theta}_i$ can be seen as an indirect measure of the power reserve for the ith turbine.
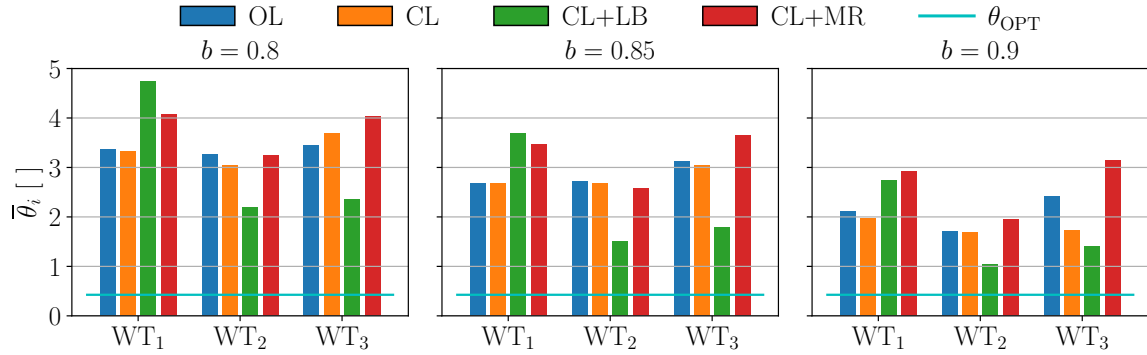
Figure 24. Mean collective blade pitch angle $\overline{\overline{\theta}}$ for the four APC algorithms and three power demand levels b. Experiment with dynamic wind direction variations.

Results show that CL+LB presents a significantly unbalanced power reserve distribution, shifted towards the upstream rotor, possibly as a result of the CLD loop. This is in agreement with the other quantities presented and discussed earlier in this section. As expected, CL+MR presents a rather large power reserve for all rotors, especially for WT_3, thanks to wake steering, but also for WT_1, which is remarkable since this upstream turbine is often misaligned.

455 ## 6.2 Loads and fatigue

Figure 25 presents the mean load-balancing error for the dynamic turntable experiment.
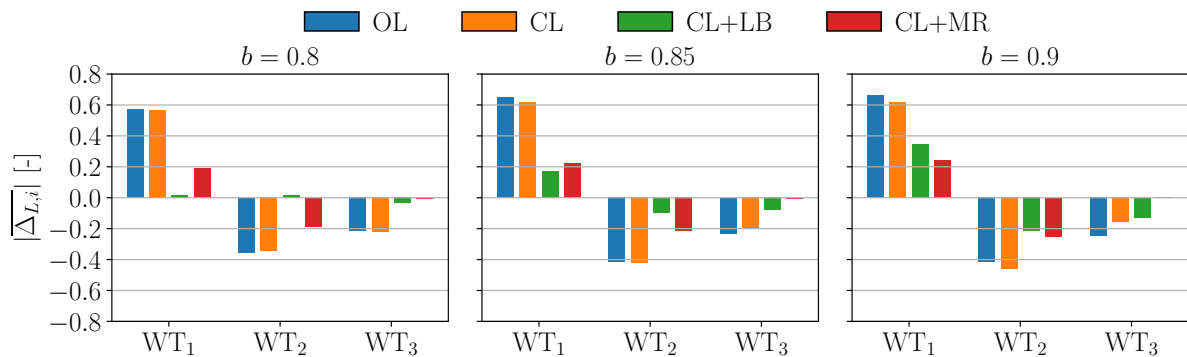
Figure 25. Mean local load balancing error for tower-base fore-aft bending for the four APC algorithms and three power demand levels b. The error is normalized by $\frac{1}{2}\rho U_\infty^2$. Positive values indicate loading above the wind farm average. Experiment with dynamic wind direction variations.

For OL and CL, the front turbine WT_1 exhibits the highest loading, which progressively diminishes for rotors located further downstream. As seen already in the static cases, CL+LB effectively balances the loads. Its effectiveness is excellent at $b = 0.8$ but – importantly – gradually deteriorates as b increases since more saturation events arise that modify the power share distribution to prioritize tracking accuracy. CL+MR displays the second-best performance for the lower b values, but ultimately outperforms CL+LB for $b = 0.9$. This shows the importance of controlling saturations, and the limits of a purely load balancing strategy.

Figure 26 reports the normalized tower-base fore-aft DELs.
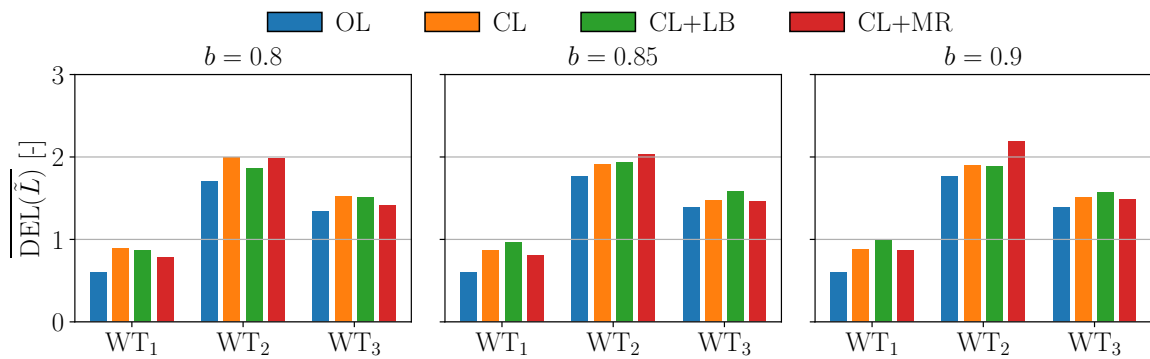
Figure 26. Tower-base fore-aft DELs for the four APC algorithms and three power demand levels b. DELs are normalized by $\frac{1}{2}\rho U_\infty^2$. Experiment with dynamic wind direction variations.

These results generally indicate a higher fatigue for WT_2, followed by WT_3 and WT_1, which is the least affected turbine. WT_2 is also the rotor that generally has the smallest power margin in the farm, as shown in Fig. 24. This result is consistent with the findings of Tamaro et al. (2025b), which showed that fatigue is driven by the low-frequency load cycles that occur because of saturation events. OL generally exhibits the lowest fatigue, due to the smoother control of the rotors. The proposed CL+MR method reduces $\overline{\mathrm{DEL}(\tilde{L})}$ for WT_1 and WT_3 compared to other methods featuring a closed loop, while it increases it for WT_2, possibly due to a lower power margin deriving from the α_i and γ_i LUTs.

7   Conclusions

A maximum-reserve approach for robust wind farm power tracking that combines wake steering and induction control has been tested experimentally in a wind tunnel. The objective of the algorithm is to enhance power reserves across the wind farm to mitigate the effects of wind lulls, thereby generating a more accurate tracking of the desired power signal.

To support the experimental work, a steady-state model was developed, based on a modified version of FLORIS. This model accounts for the aerodynamic interactions resulting from simultaneous yaw misalignment and curtailed operation, as well as specific wind tunnel inflow characteristics and chord-based Reynolds number effects caused by the small scale of the turbines.

The experiments were conducted in a large boundary-layer wind tunnel using a small cluster of three scaled rotors with minimal blockage. The first set of experiments considered two wind farm layouts to replicate varying levels of wake impingement. A second, unprecedented set of APC experiments involved dynamically varying the wind direction using a large turntable.

480 The maximum-reserve method was compared with three alternative APC algorithms sourced from the recent literature. All controllers were implemented on a dedicated cabinet, enabling real-time communication to and from the controllers running on the individual turbines. The performance of the various controllers was evaluated in terms of power tracking accuracy, power reserves, structural loads, and fatigue.

The main findings of this study are as follows:

485 – A steady-state analysis confirms that wake impingement reduces power reserves of downstream rotors. The combined use of wake steering and induction control effectively enhances local power reserves, thereby improving overall power tracking accuracy.

– The treatment of saturation conditions significantly affects power tracking performance. The open-loop algorithm showed the poorest performance in most cases. However, introducing a simple feedback loop and a compensation strategy for 490 saturated rotors led to substantial improvements.

– Results from the dynamic wind direction experiments corroborated the findings from the fixed-direction runs, highlighting the strong potential of wake control in APC applications.

– Dispatching power setpoints to balance loads proved effective in reducing fatigue compared to both open-loop and closed-loop controllers with fixed setpoints. However, load-balancing setpoints may lead to localized saturation, partic-495 ularly at high power demand levels, which in turn negatively affects loading.

Future work may extend this study by investigating the role of curtailment strategies on power tracking performance. Another area of investigation that should be pursued is the direct inclusion of loads in the maximum-reserve formulation because, as seen here, a correct management of reserves can have major implications on loading.

Appendix A: Floris wake parameters

500 Tables A1, A2 and A3 present the values of the parameters of the wake deflection, turbulence, and wake deficit models, respectively.

Table A1. Values of the parameters of the deflection model (Bastankhah and Porté-Agel, 2014).

a_d	b_d	A	B	k_a	k_b	d_m	ϵ_{gain}
0	0	0.58	0.077	0.38	0.004	1	0.2

Table A2. Values of the parameters of the turbulence model (Crespo and Hernàndez, 1996).

Initial	Constant	a_i	Downstream
0.1057	0.3401	0.9558	-0.3562

Table A3. Values of the parameters of the Gauss deficit model (Bastankhah and Porté-Agel, 2014).

A	β	k_a	k_b
0.8647	0.1226	0.4783	0.0044

Appendix B: Blade pitch actuator duty cycle

The actuator duty cycle (ADC) of blade pitch is shown for the static turntable experiments in Figs. B1 and B2 for $\psi = 2.8°$ and $\psi = 5.7°$, respectively. ADC for the blade pitch angle θ is defined as (Bottasso et al., 2013)

$$505 \quad \mathrm{ADC}_\theta = \frac{1}{T} \int_0^T \frac{\dot{\theta}(t)}{\dot{\theta}_{\max}} \, \mathrm{d}t, \tag{B1}$$

where $\dot{\theta}$ is the pitch rate.

Results appear to be strongly dependent on the power demand level b. When $b = 0.8$, waked turbines show a higher pitch activity than the upstream turbine WT_1. This condition persists for OL and CL+MR in most of the other b scenarios and for both wind directions ψ. For CL and CL+MR, on the contrary, for $b = 0.9$ it is the front turbine WT_1 that displays the highest

510 pitch activity, most likely due to the need for compensating the saturation events happening at the downstream waked turbines. It should also be noted that when a turbine saturates, its pitch lies at $\theta = \theta_{\mathrm{OPT}}$ until the saturation criteria are not met anymore, and this automatically reduces ADC.
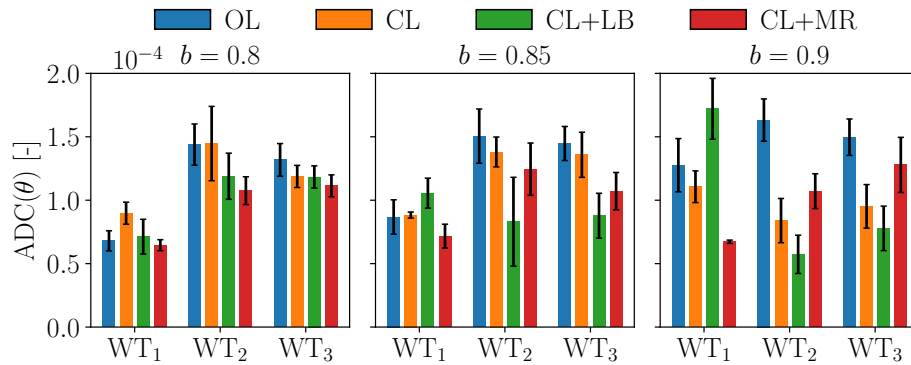
Figure B1. Blade pitch ADC for the static turntable experiment with wind direction $\psi = 2.8°$, corresponding to 75% rotor overlap. Whiskers indicate 95% confidence intervals. Results are presented for three power demand requests b.
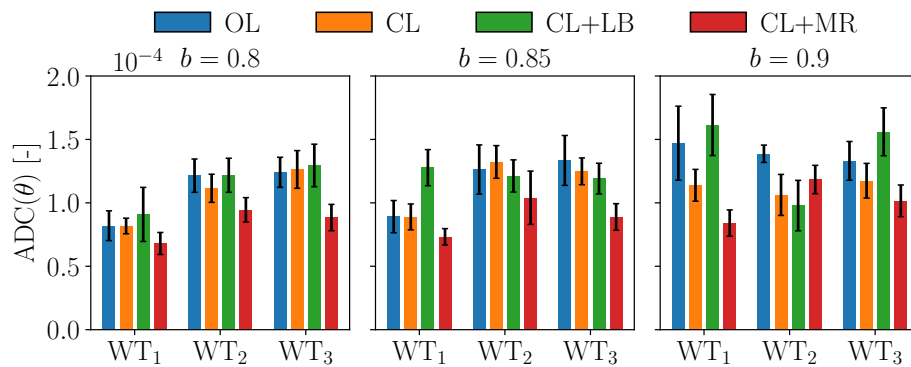
Figure B2. Blade pitch ADC for the static turntable experiment with wind direction $\psi = 5.7°$, corresponding to 50% rotor overlap. Whiskers indicate 95% confidence intervals. Results are presented for three power demand requests b.

Appendix C: Load balancing error

For completeness, Fig. C1 reports the mean local load balancing error for the case $\psi = 5.7°$ (50% rotor overlap). The case
515 $\psi = 5.7°$ (75% rotor overlap) was shown earlier in Fig. 19.
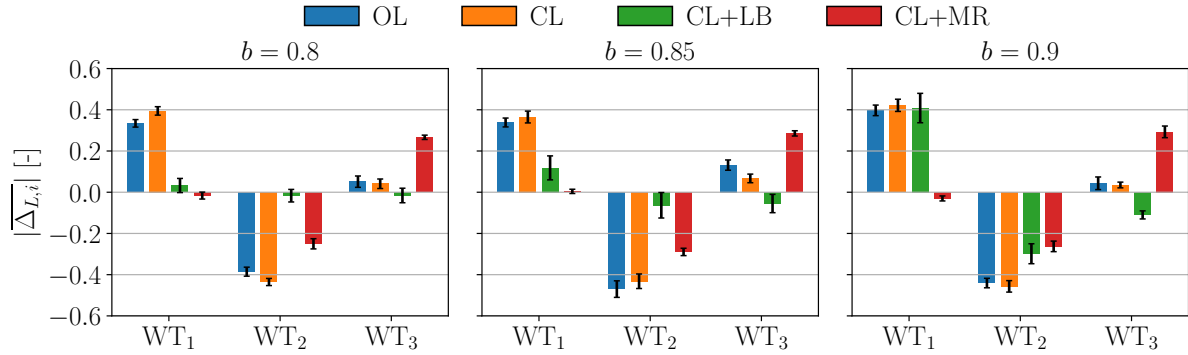
Figure C1. Mean local load balancing error for the tower-base fore-aft bending moment for the static turntable experiment with wind direction $\psi = 5.7°$, corresponding to 75% rotor overlap. L is normalized with $\frac{1}{2}\rho U_\infty^2$. Positive values indicate loading above the wind farm average. Results are presented for three power demand requests b.

Appendix D: Nomenclature

	$\mathbf{A}$	Ambient conditions
	b	Shift of normalized power demand signal (i.e. average power demand level)
	C_P	Power coefficient
520	C_T	Thrust coefficient
	c	Amplitude of normalized power demand signal
	D	Rotor diameter
	K^I	Control gain (integral)
	K^P	Control gain (proportional)
525	m	Power reserve
	N	Total number of wind turbines
	n_k^{AGC}	Normalized power demand signal
	P	Wind turbine power
	P_D	Wind turbine power demand
530	P_R	Rated power
	P_{ref}	Reference power signal
	P_{ref}^{PI}	Closed-loop, APC control output
	R	Rotor radius
	S	Number of saturated rotors
535	t	Time
	U	Rotor-equivalent wind speed
	U_∞	Freestream wind speed measured at hub height
	$\mathbf{u}$	Control inputs
540	α	Power-share setpoint
	γ	Misalignment angle
	Δ_L	Load balancing error
	Δ_P	Power tracking error
	ϵ	Auxiliary power scaling factor
545	η_P	Power loss factor
	θ	Blade pitch angle
	λ	Tip speed ratio
	ρ	Air density
	τ	Time instant index

550 | ψ | Wind direction |
Ω	Rotor angular speed
Ω_R	Rated rotor angular speed
555	AGC	Automatic generation control
APC	Active power control
CL	Closed loop
CLD	Coordinated load distribution
CL+LB	Closed loop with load balancing
CL+MR	Closed loop with maximum reserve
560	DEL	Damage equivalent load
LUT	Look-up table
FLORIS	FLOw Redirection and Induction in Steady State
OL	Open loop
PI	Proportional – integral
565	RMS	Root mean square
TI	Turbulence intensity
TSO	Transmission system operator
WF	Wind farm
WT	Wind turbine
570

Code and data availability. The Simulink models of the APC controllers, and the C++ codes generated from them are accessible in the European open repository Zenodo at https://doi.org/10.5281/zenodo.17551525 (Tamaro et al., 2025a). A video of one of the experiments is available at https://youtu.be/CIfaI2VKz2g.

Author contributions. CLB developed the formulation of the maximum-reserve APC method and supervised the overall research. ST im-
575 plemented the model, performed the experiments, and conducted the steady state analyses with FLORIS. FC coordinated the experimental campaign and supported the development and implementation of the controllers. DB and FM contributed to the wind tunnel campaign. All authors contributed to the interpretation of the results. CLB and ST wrote the paper, with contributions by FC. All authors provided important input to this research work through discussions and feedback, and improved the manuscript.

Competing interests. The authors declare that they have no conflict of interest, except for CLB, who is the Editor in Chief of the Wind Energy Science journal.

Financial support. This work has been supported in part by the PowerTracker project, which receives funding from the German Federal Ministry for Economic Affairs and Climate Action (FKZ: 03EE2036A). This work has also been partially supported by the SUDOCO project, which receives funding from the European Union's Horizon Europe Programme under grant agreement 101122256.

Acknowledgements. The authors express their gratitude to the wind tunnel team at Politecnico di Milano for providing assistance in the experiments.

References

Aho, J., Buckspan, A., Laks, J., Fleming, P., Jeong, Y., Dunne, F., Churchfield, M., Pao, L., and Johnson, K.: A tutorial of wind turbine control for supporting grid frequency through active power control, in: 2012 American Control Conference (ACC), pp. 3120–3131, https://doi.org/10.1109/ACC.2012.6315180, 2012.

590 Bachmann electronic GmbH: System overview, Bachmann electronic GmbH, Feldkirch, 2017.

Bastankhah, M. and Porté-Agel, F.: A new analytical model for wind-turbine wakes, Renewable Energy, 70, 116–123, https://doi.org/https://doi.org/10.1016/j.renene.2014.01.002, special issue on aerodynamics of offshore wind energy systems and wakes, 2014.

Boersma, S., Rostampour, V., Doekemeijer, B., van Geest, W., and van Wingerden, J.-W.: A constrained model predictive wind farm con-

595 troller providing active power control: an LES study, Journal of Physics: Conference Series, 1037, 032 023, https://doi.org/10.1088/1742-6596/1037/3/032023, 2018.

Bossanyi, E. and Ruisi, R.: Axial induction controller field test at Sedini wind farm, Wind Energy Science, 6, 389–408, https://doi.org/10.5194/wes-6-389-2021, 2021.

Bottasso, C., Campagnolo, F., Croce, A., and Tibaldi, C.: Optimization-based study of bend–twist coupled rotor blades for passive and

600 integrated passive/active load alleviation, Wind Energy, 16, 1149–1166, https://doi.org/https://doi.org/10.1002/we.1543, 2013.

Bottasso, C. L. and Campagnolo, F.: Wind tunnel testing of wind turbines and farms, in: Handbook of Wind Energy Aerodynamics, edited by Stoevesandt, B., Schepers, G., Fuglsang, P., and Sun, Y., pp. 1077–1126, Springer International Publishing, Cham, ISBN 978-3-030-31307-4, https://doi.org/10.1007/978-3-030-31307-4_54, 2022.

Bottasso, C. L., Campagnolo, F., and Petrović, V.: Wind tunnel testing of scaled wind turbine models: Beyond aerodynamics, J. Wind Eng.

605 Ind. Aerodyn, 127, 2014.

Boyle, J. and Littler, T.: A review of frequency-control techniques for wind power stations to enable higher penetration of renewables onto the Irish power system, Energy Reports, 12, 5567–5581, https://doi.org/https://doi.org/10.1016/j.egyr.2024.11.031, 2024.

Brayton, R., Director, S., Hachtel, G., and Vidigal, L.: A new algorithm for statistical circuit design based on quasi-Newton methods and function splitting, IEEE Transactions on Circuits and Systems, 26, 784–794, https://doi.org/10.1109/TCS.1979.1084701, 1979.

610 Bromm, M., Rott, A., Beck, H., Vollmer, L., Steinfeld, G., and Kühn, M.: Field investigation on the influence of yaw misalignment on the propagation of wind turbine wakes, Wind Energy, 21, 1011–1028, https://doi.org/https://doi.org/10.1002/we.2210, 2018.

Campagnolo, F., Petrović, V., Schreiber, J., Nanos, E. M., Croce, A., and Bottasso, C. L.: Wind tunnel testing of a closed-loop wake deflection controller for wind farm power maximization, Journal of Physics: Conference Series, 753, 032 006, https://doi.org/10.1088/1742-6596/753/3/032006, 2016.

615 Campagnolo, F., Weber, R., Schreiber, J., and Bottasso, C. L.: Wind tunnel testing of wake steering with dynamic wind direction changes, Wind Energy Science, 5, 1273–1295, https://doi.org/10.5194/wes-5-1273-2020, 2020.

Campagnolo, F., Castellani, F., Natili, F., Astolfi, D., and Mühle, F.: Wind tunnel testing of yaw by individual pitch control applied to wake steering, Frontiers in Energy Research, 10, https://doi.org/10.3389/fenrg.2022.883889, 2022a.

Campagnolo, F., Imširović, L., von Braunbehrens, R., and Bottasso, C. L.: Further calibration and validation of FLORIS with wind tunnel

620 data, Journal of Physics: Conference Series, 2265, 022 019, https://doi.org/10.1088/1742-6596/2265/2/022019, 2022b.

Canet, H., Bortolotti, P., and Bottasso, C.: On the scaling of wind turbine rotors, Wind Energy Science, 6, 601–626, https://doi.org/10.5194/wes-6-601-2021, 2021.

Cossu, C.: Wake redirection at higher axial induction, Wind Energy Science, 6, 377–388, https://doi.org/10.5194/wes-6-377-2021, 2021.

Crespo, A. and Hernàndez, J.: Turbulence characteristics in wind-turbine wakes, Journal of Wind Engineering and Industrial Aerodynamics,
625   61, 71–85, https://doi.org/https://doi.org/10.1016/0167-6105(95)00033-X, 1996.

Doekemeijer, B. M., Kern, S., Maturu, S., Kanev, S., Salbert, B., Schreiber, J., Campagnolo, F., Bottasso, C. L., Schuler, S., Wilts, F.,
Neumann, T., Potenza, G., Calabretta, F., Fioretti, F., and van Wingerden, J.-W.: Field experiment for open-loop yaw-based wake steering
at a commercial onshore wind farm in Italy, Wind Energy Science, 6, 159–176, https://doi.org/10.5194/wes-6-159-2021, 2021.

Ela, E., Gevorgian, V., Fleming, P., Zhang, Y. C., Singh, M., Muljadi, E., Scholbrook, A., Aho, J., Buckspan, A., Pao, L., Singhvi, V., Tuohy,
630   A., Pourbeik, P., Brooks, D., and Bhatt, N.: Active power controls from wind power: bridging the gaps, Tech. Rep. NREL/TP-5D00-60574,
National Renewable Energy Lab. (NREL), https://doi.org/10.2172/1117060, 2014.

Fleming, P., Aho, J., Gebraad, P., Pao, L., and Zhang, Y.: Computational fluid dynamics simulation study of active power control in wind
plants, in: 2016 American Control Conference (ACC), pp. 1413–1420, https://doi.org/10.1109/ACC.2016.7525115, 2016.

Fleming, P., King, J., Dykes, K., Simley, E., Roadman, J., Scholbrock, A., Murphy, P., Lundquist, J. K., Moriarty, P., Fleming, K., van Dam,
635   J., Bay, C., Mudafort, R., Lopez, H., Skopek, J., Scott, M., Ryan, B., Guernsey, C., and Brake, D.: Initial results from a field campaign
of wake steering applied at a commercial wind farm – Part 1, Wind Energy Science, 4, 273–285, https://doi.org/10.5194/wes-4-273-2019,
2019.

Frederik, J. A., Doekemeijer, B. M., Mulders, S. P., and van Wingerden, J.-W.: The helix approach: using dynamic individual pitch control
to enhance wake mixing in wind farms, Wind Energy, 23, 1739–1751, https://doi.org/https://doi.org/10.1002/we.2513, 2020a.

640   Frederik, J. A., Weber, R., Cacciola, S., Campagnolo, F., Croce, A., Bottasso, C., and van Wingerden, J.-W.: Periodic dynamic induc-
tion control of wind farms: proving the potential in simulations and wind tunnel experiments, Wind Energy Science, 5, 245–257,
https://doi.org/10.5194/wes-5-245-2020, 2020b.

Gonzalez Silva, J., Doekemeijer, B. M., Ferrari, R., and van Wingerden, J.-W.: Active power control of wind farms: an instantaneous approach
on waked conditions, Journal of Physics: Conference Series, 2265, 022 056, https://doi.org/10.1088/1742-6596/2265/2/022056, 2022.

645   Gonzalez Silva, J., van der Hoek, D., Ferrari, R., and van Wingerden, J. W.: Wind tunnel testing of wind turbine and wind farm control
strategies for active power regulation, Journal of Renewable and Sustainable Energy, 16, 053 302, https://doi.org/10.1063/5.0215493,
2024.

Heck, K., Johlas, H., and Howland, M.: Modelling the induction, thrust and power of a yaw-misaligned actuator disk, Journal of Fluid
Mechanics, 959, A9, https://doi.org/10.1017/jfm.2023.129, 2023.

650   Howland, M. F., Lele, S. K., and Dabiri, J. O.: Wind farm power optimization through wake steering, Proceedings of the National Academy
of Sciences, 116, 14 495–14 500, https://doi.org/10.1073/pnas.1903680116, 2019.

Jensen, N.: A note on wind generator interaction, no. 2411 in Risø-M, Risø National Laboratory, ISBN 87-550-0971-9, 1983.

Jiménez, A., Crespo, A., and Migoya, E.: Application of a LES technique to characterize the wake deflection of a wind turbine in yaw, Wind
Energy, 13, 559–572, https://doi.org/https://doi.org/10.1002/we.380, 2010.

655   Liew, J. and Larsen, G. C.: How does the quantity, resolution, and scaling of turbulence boxes affect aeroelastic simulation convergence?,
Journal of Physics: Conference Series, 2265, 032 049, https://doi.org/10.1088/1742-6596/2265/3/032049, 2022.

Lin, M. and Porté-Agel, F.: Wake meandering of wind turbines under dynamic yaw control and impacts on power and fatigue, Renewable
Energy, 223, 120 003, https://doi.org/https://doi.org/10.1016/j.renene.2024.120003, 2024.

Meyers, J., Bottasso, C. L., Dykes, K., Fleming, P., Gebraad, P., Giebel, G., Göçmen, T., and van Wingerden, J.-W.: Wind farm flow control:
660   prospects and challenges, Wind Energy Science Discussions, https://doi.org/https://doi.org/10.5194/wes-2022-24, 2022.

Mühle, F. V., Heckmeier, F. M., Campagnolo, F., and Breitsamter, C.: Wind tunnel investigations of an individual pitch control strategy for wind farm power optimization, Wind Energy Science, 9, 1251–1271, https://doi.org/10.5194/wes-9-1251-2024, 2024.

Munters, W. and Meyers, J.: Towards practical dynamic induction control of wind farms: analysis of optimally controlled wind-farm boundary layers and sinusoidal induction control of first-row turbines, Wind Energy Science, 3, 409–425, https://doi.org/10.5194/wes-3-409-2018, 2018.

Nanos, E. M., Bottasso, C. L., Tamaro, S., Manolas, D. I., and Riziotis, V. A.: Vertical wake deflection for floating wind turbines by differential ballast control, Wind Energy Science, 7, 1641–1660, https://doi.org/10.5194/wes-7-1641-2022, 2022.

National Renewable Energy Laboratory: NREL/floris: v3.0, Zenodo, https://doi.org/10.5281/zenodo.6320841, 2022.

Oudich, Y., Gyselinck, J., De Belie, F., and Kinnaert, M.: Providing power reserve for secondary grid frequency regulation of offshore wind farms through yaw control, Wind Energy, 26, 850–873, https://doi.org/https://doi.org/10.1002/we.2845, 2023.

Petrović, V., Schottler, J., Neunaber, I., Hölling, M., and Kühn, M.: Wind tunnel validation of a closed loop active power control for wind farms, Journal of Physics: Conference Series, 1037, 032 020, https://doi.org/10.1088/1742-6596/1037/3/032020, 2018.

Porté-Agel, F., Wu, Y.-T., and Chen, C.-H.: A numerical study of the effects of wind direction on turbine wakes and power losses in a large wind farm, Energies, 6, 5297–5313, https://doi.org/10.3390/en6105297, 2013.

Profibus Nutzerorganisation e. V. (PNO): Profinet system – Description technology and application, Profibus & Profinet International (PI), Haid-und-Neu-Str. 7, 76131 Karlsruhe, Germany, 4 edn., 2018.

Shapiro, C. R., Bauweraerts, P., Meyers, J., Meneveau, C., and Gayme, D. F.: Model-based receding horizon control of wind farms for secondary frequency regulation, Wind Energy, 20, 1261–1275, https://doi.org/https://doi.org/10.1002/we.2093, 2017.

Starke, G. M., Meneveau, C., King, J., and Gayme, D. F.: Yaw-augmented control for wind farm power tracking, in: 2023 American Control Conference (ACC), pp. 184–191, https://doi.org/10.23919/ACC55779.2023.10156444, 2023.

Tamaro, S. and Bottasso, C. L.: A new wind farm active power control strategy to boost tracking margins in high-demand scenarios, in: 2023 American Control Conference (ACC), pp. 192–197, https://doi.org/10.23919/ACC55779.2023.10156275, 2023.

Tamaro, S., Campagnolo, F., and Bottasso, C. L.: On the power and control of a misaligned rotor – Beyond the cosine law, Wind Energy Science, 9, 1547–1575, https://doi.org/10.5194/wes-9-1547-2024, 2024a.

Tamaro, S., Guilloré, A., Anand, A., Mühle, F. V., Campagnolo, F., and Bottasso, C. L.: Validation of induction/steering reserve-boosting active power control by a wind tunnel experiment with dynamic wind direction changes, Journal of Physics: Conference Series, 2767, 092 067, https://doi.org/10.1088/1742-6596/2767/9/092067, 2024b.

Tamaro, S., Bortolin, D., Campagnolo, F., Mühle, F. V., and Bottasso, C. L.: Scaled testing of maximum-reserve active power control, Zenodo [source code and data set], https://doi.org/10.5281/zenodo.17551525, 2025a.

Tamaro, S., Campagnolo, F., and Bottasso, C. L.: A robust active power control algorithm to maximize wind farm power tracking margins in waked conditions, Wind Energy Science Discussions, 2025, 1–31, https://doi.org/10.5194/wes-2025-66, 2025b.

The MathWorks, Inc.: MATLAB, Version 9.13.0 (R2022b), https://www.mathworks.com, computer software, 2022.

Vali, M., Petrović, V., Steinfeld, G., Y. Pao, L., and Kühn, M.: An active power control approach for wake-induced load alleviation in a fully developed wind farm boundary layer, Wind Energy Science, 4, 139–161, https://doi.org/10.5194/wes-4-139-2019, 2019.

van der Hoek, D., Kanev, S., Allin, J., Bieniek, D., and Mittelmeier, N.: Effects of axial induction control on wind farm energy production – A field test, Renewable Energy, 140, 994–1003, https://doi.org/https://doi.org/10.1016/j.renene.2019.03.117, 2019.

van Wingerden, J.-W., Pao, L., Aho, J., and Fleming, P.: Active power control of waked wind farms, IFAC-PapersOnLine, 50, 4484–4491, https://doi.org/https://doi.org/10.1016/j.ifacol.2017.08.378, 20th IFAC World Congress, 2017.

von Braunbehrens, R., Vad, A., and Bottasso, C. L.: The wind farm as a sensor: learning and explaining orographic and plant-induced flow heterogeneities from operational data, Wind Energy Science, 8, 691–723, https://doi.org/10.5194/wes-8-691-2023, 2023.

Wang, C., Campagnolo, F., and Bottasso, C. L.: Identification of airfoil polars from uncertain experimental measurements, Wind Energy Science, 5, 1537–1550, https://doi.org/10.5194/wes-5-1537-2020, 2020.

Wang, C., Campagnolo, F., Canet, H., Barreiro, D. J., and Bottasso, C. L.: How realistic are the wakes of scaled wind turbine models?, Wind Energy Science, 6, 961–981, https://doi.org/10.5194/wes-6-961-2021, 2021.